PAPER • OPEN ACCESS

Density fluctuation correlation measurements in ASDEX Upgrade using poloidal and radial correlation reflectometry

To cite this article: D Prisiazhniuk *et al* 2018 *Plasma Phys. Control. Fusion* **60** 075003

View the article online for updates and enhancements.

Related content

- Magnetic field pitch angle and perpendicular velocity measurements from multi-point time-delay estimation of poloidal correlation reflectometry
D Prisiazhniuk, A Krämer-Flecken, G D Conway et al.

- Radial correlation length measurements on ASDEX Upgrade
J Schirmer, G D Conway, E Holzhauer et al.

- Density profile and turbulence evolution during L-H transition studied with the ultra-fast swept reflectometer on ASDEX Upgrade
A Medvedeva, C Bottereau, F Clairet et al.

Recent citations

- Nonlinear Doppler reflectometry power response. Analytical predictions and full-wave modelling
O L Krutkin *et al*

IOP ebooks™

Bringing you innovative digital publishing with leading voices to create your essential collection of books in STEM research.

Start exploring the collection - download the first chapter of every title for free.

Erratum: Density fluctuation correlation measurements in ASDEX Upgrade using poloidal and radial correlation reflectometry (2018 *Plasma Phys. Control. Fusion* **60 075003**)

D Prisiazhniuk[1,2] , **G D Conway**[1], **A Krämer-Flecken**[3] , **U Stroth**[1,2] **and the ASDEX Upgrade Team**

[1] Max-Planck-Institut für Plasmaphysik, Boltzmannstraße 2, D-85748 Garching, Germany
[2] Physik-Department E28, Technische Universität München, D-85748 Garching, Germany
[3] Institut für Energieforschung—Plasmaphysik, Forschungszentrum Jülich, Germany

E-mail: dmitrii.prisiazhniuk@ipp.mpg.de

(Some figures may appear in colour only in the online journal)

There was a publishing error introduced during the processing of figures 5 and 19. The font and labels of these figures have been corrupted. A corrected version of these figures have been provided below. In the published version of figure 13, there was a compilation error in the display of the labels; this error does not affect the results shown in figure 13.
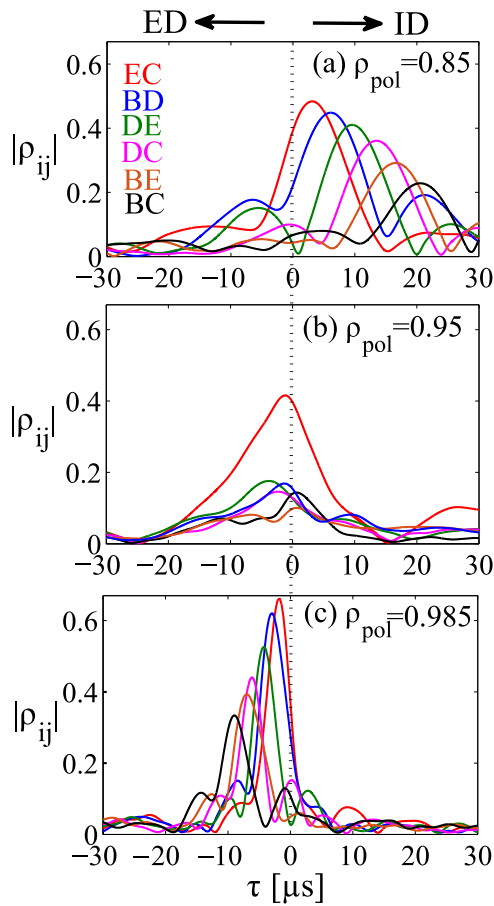
Figure 5. The measured cross-correlation functions (a) in the outer core, (b) in the pedestal, and (c) in the E_r well region of the L-mode plasma of #31 427.

On page 2, the sentence '…where ε is the separation between measurement points…', should instead read '…where $\varepsilon_{\perp}$ is the separation between measurement points…'.
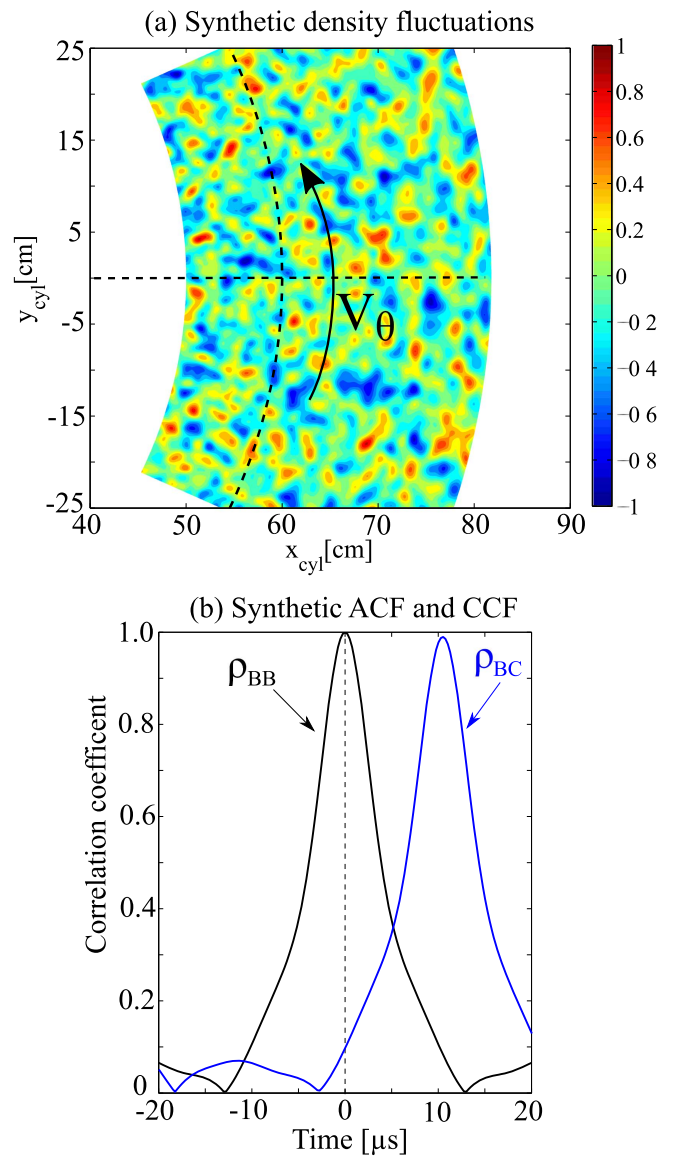

Figure 19. (a) Example of a synthetic density fluctuation snapshot used in the simulations. (b) The auto- (black) and cross- (blue) correlation functions of synthetic PCR signal.

ORCID iDs

D Prisiazhniuk ⓘ https://orcid.org/0000-0002-0249-8397
A Krämer-Flecken ⓘ https://orcid.org/0000-0003-4146-5085

Density fluctuation correlation measurements in ASDEX Upgrade using poloidal and radial correlation reflectometry

D Prisiazhniuk[1,2] , **G D Conway**[1], **A Krämer-Flecken**[3] , **U Stroth**[1,2] and the **ASDEX Upgrade Team**

[1] Max-Planck-Institut für Plasmaphysik, Boltzmannstraße 2, D-85748 Garching, Germany
[2] Physik-Department E28, Technische Universität München, D-85748 Garching, Germany
[3] Institut für Energieforschung—Plasmaphysik, Forschungszentrum Jülich, Germany

E-mail: dmitrii.prisiazhniuk@ipp.mpg.de

Abstract

The poloidal correlation reflectometry diagnostic operated in ordinary mode with additional radial correlation channel is applied in this paper to investigate the correlation of the turbulent density fluctuations. The perpendicular and radial correlation lengths, $l_\perp$ and l_r, the perpendicular velocity $v_\perp$ and the dissipation (mutation) time τ_d are measured simultaneously from the outer core to edge in the L-mode plasmas of ASDEX Upgrade. It is shown that in the outer core region ($0.6 < \rho_{\rm pol} < 0.9$) the measured correlation lengths scale with the drift wave length, $l_\perp \approx 5\rho_s$ and $l_r \approx 10\rho_s$, while the dissipation time is inversely correlated with the velocity $\tau_d \approx 40/v_\perp$ (τ_d is in μs and $v_\perp$ in km s^{-1}). In the pedestal region ($0.925 < \rho_{\rm pol} < 0.98$), where the $E \times B$ shear flows are present, a loss of measured correlation is observed which can be explained by a combination of small propagation velocity and an additional reduction of τ_d. In the E_r well region ($\rho_{\rm pol} \approx 0.99$), the measured perpendicular correlation length increases $l_\perp \approx 13\rho_s$ and the radial correlation length decreases $l_r \approx 4\rho_s$ compared to the outer core values. The correlation measurements are interpreted in the frame of the linear regime of reflectometry (applied only to $\rho_{\rm pol} < 0.9$). Using the Born approximation we show that the finite wavenumber sensitivity of the reflectometer increases the measured $l_\perp$ and l_r, but does not affect the measured τ_d. By the including diagnostic correction the real correlation lengths $l_\perp \approx l_r \approx 3\rho_s$ are estimated.

Keywords: poloidal correlation reflectometry, turbulence, correlation, velocity shear

(Some figures may appear in colour only in the online journal)

1. Introduction

The study of the mechanisms governing turbulent fluctuations is crucial for the understanding of plasma confinement. Beside probes and laser based diagnostics, microwave reflectometry diagnostics [1] are sensitive enough to measure turbulent density fluctuations with high spatio-temporal resolution. This method is based on the measurement of the reflected microwave beam from a cut-off layer in the plasma which depends on polarization mode (O- or X-mode) and probing frequency (f). Variations in the phase of the reflected beam is related to movements in the density cutoff iso-layers, from which density fluctuations can be estimated. To quantify how turbulent density fluctuations at one location and one time point correlate with those at another location and time a cross-correlation analysis can be applied.

Several different approaches are possible to measure the correlation of turbulent density fluctuations using reflecto-metry. In a radial correlation reflectometry scheme, signals at
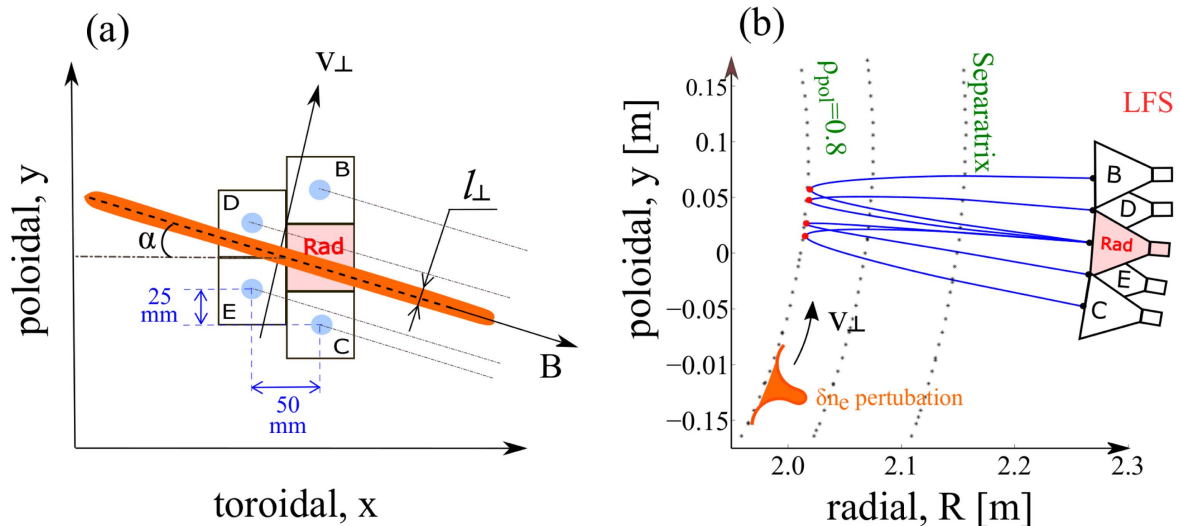
Figure 1. (a) Schematic of the PCR antenna array on ASDEX Upgrade. Rad (red) is transmitting while B, D, E, C (blue) are receiving antennas. A turbulent eddy (orange) of perpendicular size $l_\perp$ aligned parallel to the magnetic field moves in the perpendicular direction in front of the PCR antennas. (b) Example of ray tracing calculations used to obtain the reflection positions.

two different probing frequencies (f_1 and f_2) are measured simultaneously. Since the reflection layers have a radial separation, this method provides a measurement of the radial correlation length l_r from the decay of the cross-correlation coefficient. The application of normal incidence radial correlation reflectometry [2–4] and Doppler radial correlation reflectometry (i.e. with oblique incidence) [5] have shown that measured radial correlation length scale as $l_r \approx C\rho_s$, where $\rho_s = \sqrt{T_e m_i}/eB$ is the drift wave length, T_e the electron temperature, m_i the ion mass, e the elementary charge and B the magnetic field. The coefficient C has been reported in different works to be measured between 5 and 12. Note that normal incidence reflectometry in the linear regime can suffer from small angle scattering contribution [6, 7], which increases the measured radial correlation length.

Alternatively, signals can be measured at the same reflection layer, but with two or more poloidally or toroidally separated antennas. Since it is generally expected that density fluctuations are aligned along the magnetic field lines with a perpendicular to parallel correlation length ratio $l_\perp/l_\parallel < 10^{-2}$ [8–10], their parallel propagation can be neglected if parallel to the perpendicular velocity ratio $v_\parallel/v_\perp < 10^2$ [11]. Hence the cross-correlation between separated antennas can be used to obtain the perpendicular velocity $v_\perp$, the perpendicular correlation length $l_\perp$ and the dissipation (mutation) time τ_d of turbulent density fluctuations. Note that if the separation between antennas is too long, density fluctuations decorrelate during propagation. Hence, $\varepsilon_\perp < v_\perp \tau_d$ should be fulfilled, where ε is the separation between measurement points in perpendicular to magnetic field direction. The poloidal correlation reflectometry (PCR) scheme was first used on the JET [12, 13] and T-10 [14, 15] tokamaks with two receiving antennas. Later at TEXTOR a four receiving antenna system was used [16, 17]. Recently PCR systems have been installed on the EAST tokamak [18] and the W7-X stellarator [19, 20]. A theoretical analysis of PCR capabilities has been also analysed using a 3D WKB approach [21] only.

In this work a recently installed heterodyne PCR diagnostic on ASDEX Upgrade (AUG) [11, 22, 23] with an additional radial correlation channel is used to study the dissipation time τ_d, the perpendicular correlation length $l_\perp$ and the radial correlation length l_r of turbulent density fluctuations. The turbulence investigations were performed in L-mode plasmas for a wide range of plasma parameters. The obtained measurements are interpreted using a transfer function of the reflectometry in the Born approximation. The paper is organized as follows: in section 2 the PCR diagnostic at AUG is introduced. Typical fluctuation spectra and cross-correlation functions (CCF) from both outer core and edge regions are shown. The influence of the $E \times B$ shear flow on the CCF level is presented. In section 3, measurements of the dissipation time for different plasma parameters in L-mode plasmas are presented, while the correlation lengths are studied in section 4. The results are compared with theoretical predictions. In section 5, the limitation of the measurements are discussed using a transfer function of reflectometry in the Born approximation. We show that the finite wavenumber sensitivity of the reflectometer increases the effective measured correlation length, but does not affect the dissipation time measurements. The last section summarizes the results and presents an outlook for future studies.

2. The cross-correlation measurements

2.1. Poloidal correlation reflectometry at AUG

The heterodyne PCR diagnostic at AUG measures the reflected microwave beam with a cluster of 4 square receiving antennas, distributed poloidally and toroidally with respect to the launching antenna. Figure 1(a) shows schematically the PCR antenna array installed at the low field side midplane of AUG, where Rad is the transmitting (Tx) antenna and B, D, E, C are receiving (Rx) antennas. The separation between

receiving antenna orifices amounts to (25, 50, 75, 100) mm in the poloidal direction and (0, 50) mm in the toroidal direction respectively. All antennas lines of sight are aligned to focus to the same point (magnetic axis) at a major radius $R = 1.6$ m. The actual reflection position for each Tx/Rx antenna pair is calculated using a ray tracing approach—which is explained in detail in reference [11]. Although the ray tracing solution may be not precise close to the cut-off layer, it gives a good approximation for the maximum of reflection when compared to full-wave simulation (see section 5) or full-wave analytic solution [24, 25]. Figure 1(b) shows an example of ray tracing (blue lines) and the reflection positions (red points) for all receiving antennas. The separation between reflection positions also depends on the cut-off layer curvature due to wave refraction [11] and is thus calculated for every plasma radius.

The turbulent structures in a tokamak are strongly elongated in the direction of the helical magnetic field, i.e. they have an inclination angle α with respect to the toroidal direction [11] (see figure 1(a)). Therefore, the important separation between the detection volumes is not poloidal one, but the one perpendicular to the magnetic field line, which is calculated as

$$\varepsilon_\perp(\Delta x, \Delta y, \alpha) = (\Delta y + \Delta x \tan(\alpha))\cos(\alpha), \qquad (1)$$

where Δy and Δx denote the separation between detecting volumes in the poloidal and toroidal directions, respectively, and α denotes the magnetic field pitch angle. Note that $\varepsilon_\perp$ for combinations EC and BD, or DC and BE are different due to the change of sign of the Δx (see figure 1(a)).

The PCR at AUG uses low noise dual channel microwave synthesizers (-150 dBc Hz^{-1} wide-band noise) as the microwave radiation sources, which can operate in a fast frequency stepping mode with a transient switching time <60 μs. Hence, different plasma cut-off radii can be scanned in a short time scale. The system operates simultaneously over both the extended Ka- (24–37 GHz) and U-band (40–57 GHz) in O-mode polarization. In this work two regimes of PCR operation were used. In the first regime, the frequency of the Ka- and U-band channels were kept fixed during the plasma discharge, while a density ramp was performed. Due to the dependence of the reflection position on density the radial position is therefore scanned. In the second regime, the density is held constant, while the launch probe frequencies are stepped. A frequency step duration of 10 ms was sufficient to obtain a statistically significant CCF. Further details on the system and typical frequency programme can be found in references [11, 22, 23]. The received quadrature I/Q detector signals are digitized using a 2 MHz serial ADC with 12 bit resolution. The measured complex signal includes both amplitude and phase of the reflected signal $s(t) = I(t) + iQ(t) = A(t)e^{i\phi(t)}$.

Recently, a radial channel was also added to the Ka-band PCR system. In this new configuration the PCR transmits simultaneously two frequencies (f_1 and f_2). The receiving antennas B, D and E measure the reflected signal at the frequency f_1, while the receiving antenna C measures the reflected signal at the frequency f_2 (see figure 1(b)). With a variation of the frequency difference $\Delta f = f_2 - f_1$ the radial separation ε_r can be scanned. This approach permits the
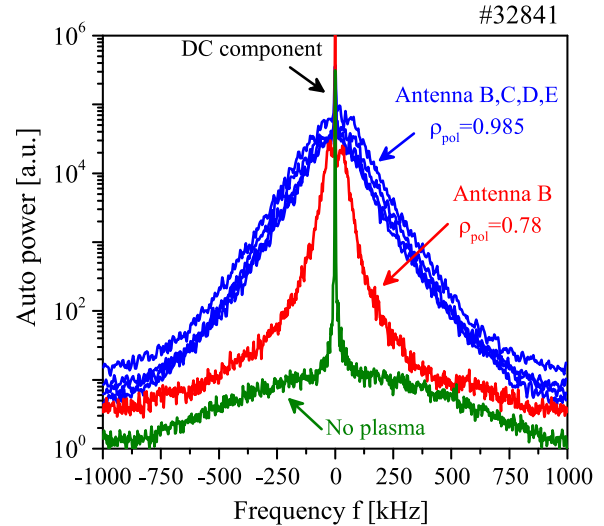

Figure 2. The typical measured power fluctuation spectra of complex signal $s(t)$ from the edge (blue) and outer core (red) regions of the L-mode plasmas. The green line shows the measured spectra without plasma.

measurement of correlations simultaneously in the perpendicular and radial directions.

2.2. Typical spectra and CCF

Figure 2 shows typical fluctuation power spectra of the complex signal $s(t)$ from the normalized radii $\rho_{pol} = 0.985$ (antennas B, C, D, E) and 0.78 (antenna B) of the Ohmic L-mode plasma discharge #32 841 (magnetic field $B_{T0} = -2.4$ T, plasma current $I_P = 0.6$ MA and line averaged electron density $n_{e0} = 2.6 \times 10^{19}$ m^{-3}). The measured spectra are usually similar for different antennas. The different widths at $\rho_{pol} = 0.985$ and 0.78 are mainly due to different rotation velocity. As shown below the velocity at $\rho_{pol} = 0.985$ is higher than at 0.78 resulting in wider frequency spectra.

The auto- and cross-correlation functions (ACF and CCF) for two discrete zero mean complex signals s_i and s_j from arbitrary PCR antenna pairs are calculated using

$$\rho_{ij}(\tau) = \frac{\langle s_i(t) \cdot s_j^\star(t + \tau)\rangle}{\sqrt{\langle |s_i(t)|^2\rangle \langle |s_j(t + \tau)|^2\rangle}}, \qquad (2)$$

where τ is a time delay between the two signals. The DC component of the signals (see figure 2) was removed before calculating the correlation functions using high pass filter (>2 kHz). Figure 3(a) shows the ACF of different receiving antennas (black lines) measured in the edge region ($\rho_{pol} = 0.985$) of L-mode discharge #32 843 ($B_{T0} = -2.4$ T, $I_P = 0.8$ MA, $n_{e0} = 2.9 \times 10^{19}$ m^{-3}). The ACF can be fitted with a Gaussian function $\rho_a(\tau) = \exp(-\tau^2/\tau_a^2)$ (red line), where τ_a is the autocorrelation time. Figure 3(b) shows CCF between different antenna pairs. The CCF varies with the antenna pair due to the different perpendicular separations $\varepsilon_\perp$. Two points should be emphasized: (i) the time delay of the maximum correlation $\tau_m(\varepsilon_\perp) = \arg \max_\tau(|\rho_{ij}(\tau)|)$ increases with separation $\varepsilon_\perp$ due to the propagation of the density fluctuations and (ii) the maximum correlation level
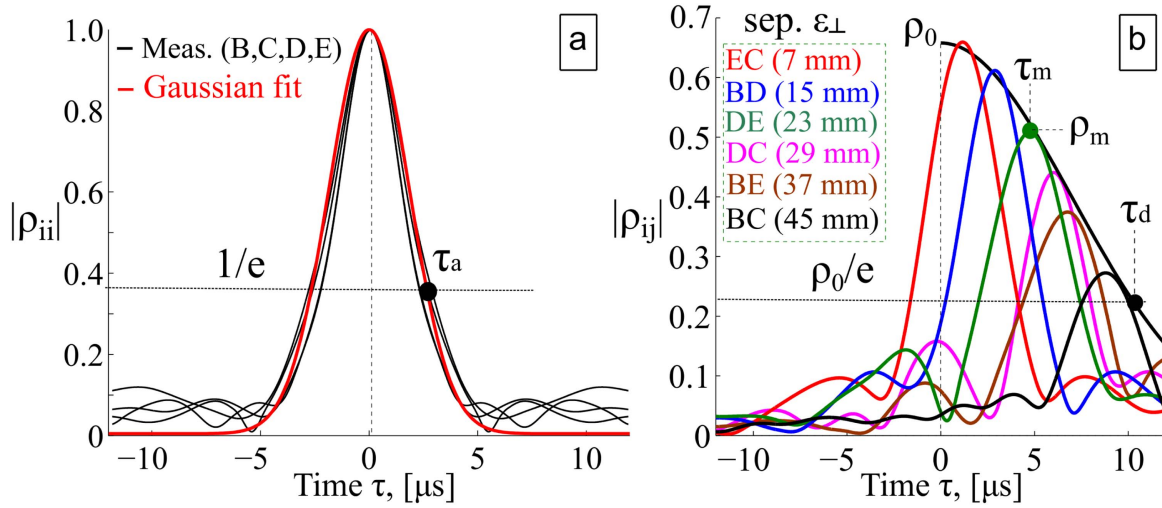
Figure 3. (a) Fit of experimental autocorrelation functions from different antennas (black) with a Gaussian function (red). (b) Cross-correlation functions for various antenna $\varepsilon_\perp$ separations.

$\rho_m = \max_\tau(|\rho_{ij}(\tau)|)$ decreases with $\varepsilon_\perp$ due to the dissipation of the turbulent structures during their propagation. It is important to note that all individual CCFs can be fitted with a Gaussian model [11]

$$\rho(\varepsilon_\perp, \tau) = \rho_0 \exp\left(-\frac{(\varepsilon_\perp - v_\perp\tau)^2}{l_{\perp,\text{eff}}^2} - \frac{\tau^2}{\tau_d^2}\right). \quad (3)$$

Here, $v_\perp$ is the perpendicular propagation velocity, τ_d the dissipation time (lifetime) of the turbulent structures and $l_{\perp,\text{eff}}$ an effective perpendicular correlation length which has contributions from both the actual perpendicular correlation length $l_\perp$ of the turbulent density fluctuations and the wavenumber sensisitivy of diagnostic. The finite wavenumber sensitivity of reflectometry acts as low pass filter in wavenumber space and is important for the interpretation of the turbulence correlation length measurement, as shown in section 5. In equation (3) we also introduce a correlation coefficient ρ_0, which differs from unity and is probably related to the presence of uncorrelated signal (noise) in the data (e.g. electronic noise in the *IQ* detectors). It is assumed that this contribution does not affect the measurements because all antenna pair combinations have approximately similar levels of noise.

In the following analyses it is important to discuss two elements: (i) the dissipation time in equation (3) is longer than the autocorrelation time defined as $\rho(0, \tau_a) = \rho(0, 0)/e$ (figure 3(a))

$$\tau_a^{-2} = \tau_p^{-2} + \tau_d^{-2}, \quad (4)$$

where $\tau_p = l_{\perp,\text{eff}}/v_\perp$ is the propagation time of the turbulent structures crossing the measured volume and τ_d the dissipation time. For the analysed L-mode plasma discharges at AUG (excluding the pedestal region $0.925 < \rho_{\text{pol}} < 0.98$) the propagation time is much smaller than the dissipation time

($\tau_p/\tau_d \approx 0.2$–$0.25$), hence, the autocorrelation time in these regions can be approximated by $\tau_a \approx l_{\perp,\text{eff}}/v_\perp < \tau_d$. (ii) According to equation (3) the measured maximum correlation time delay

$$\tau_m(\varepsilon_\perp) = \arg\ \max_\tau(|\rho(\varepsilon_\perp, \tau)|) = \frac{\varepsilon_\perp}{v_\perp}\left(1 - \frac{\tau_a^2}{\tau_d^2}\right), \quad (5)$$

depends not only on the propagation velocity, but also on the dissipation time [11]. Therefore the correction factor $(1 - \tau_a^2/\tau_d^2)$ must be taken into account when the velocity is calculated from the maximum correlation time delay.

2.3. Radial profiles and influence of the edge localized velocity shear layer

Figure 4(a) shows the root mean square (rms) phase fluctuation level $\sigma_\phi = \sqrt{\langle(\phi - \langle\phi\rangle)^2\rangle}$ as a function of the radial position. To achieve good radial coverage with a low statistical error the probing frequency was fixed at $f = 31$ GHz while the line averaged electron density was ramped during the discharge between $n_{e0} = 1.7$ and $3.3 \times 10^{19}\,\text{m}^{-3}$. Each radial point corresponds to a $\Delta t = 75$ ms window. Typical density profiles during the density ramp are shown in figure 4(e). Although both velocity and fluctuation profiles may vary with density, the purpose here is to demonstrate characteristic profiles. The precise profiles at fixed density are shown in the following sections. The phase fluctuation level increases from the outer core towards the edge due to an increase of density fluctuation level $\sigma_\phi = C_\phi \delta n_e/n_e$, where the coefficient C_ϕ depends on the specific form of the density fluctuation spectrum [26, 27]. In the case of homogeneous turbulent density fluctuations with a Gaussian shape the coefficient is calculated as [28]

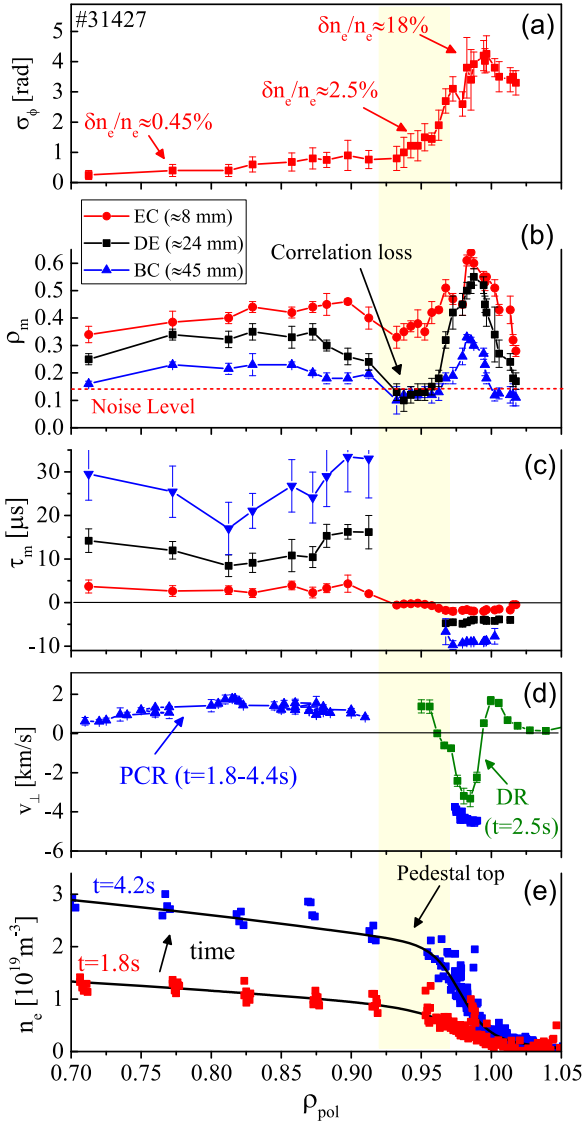$$C_\phi = k_0\sqrt{L_n l_r[\ln(L_n/l_r) + 2.2]}, \quad (6)$$

Figure 4. Radial dependence of (a) phase fluctuation level σ_ϕ, (b) maximum correlation coefficient ρ_m from different antenna combinations and (c) maximum correlation time delays τ_m. All profiles obtained using density scan from $n_{e0} = 1.7$ to 3.3×10^{19} m^{-3} at the fixed frequency 31 GHz from discharge #31 427 ($B_{T0} = -2.48$ T, $I_P = 0.8$ MA). (d) Corresponding perpendicular velocity $v_\perp$ profile from PCR and DR diagnostics. (e) Density profiles at $t = 1.8$ and 4.2 s from lithium beam and Thomson scattering diagnostics.

where $L_n = |\nabla \log(n)|^{-1}$ is the density profile scale length, k_0 the probing wavenumber and l_r the radial correlation length. This coefficient is applicable only in the linear regime of reflectometry when the density fluctuation level is small [29],

$$\left(\frac{\delta n_e}{n_e}\right)^2 < \frac{1}{k_0^2 l_r d_c} \ln\left(\frac{d_c}{l_r}\right)^{-1} \tag{7}$$

(several percent for the case of PCR at AUG) and has been tested against O-mode full-wave modelling [28]. d_c is the distance from the antenna to the cut-off layer. Using this coefficient and assuming $l_r \approx 1$ cm the fluctuation level $\delta n_e/n_e$ is calculated to vary from 0.45% at $\rho_{pol} = 0.75$ to some 18% at
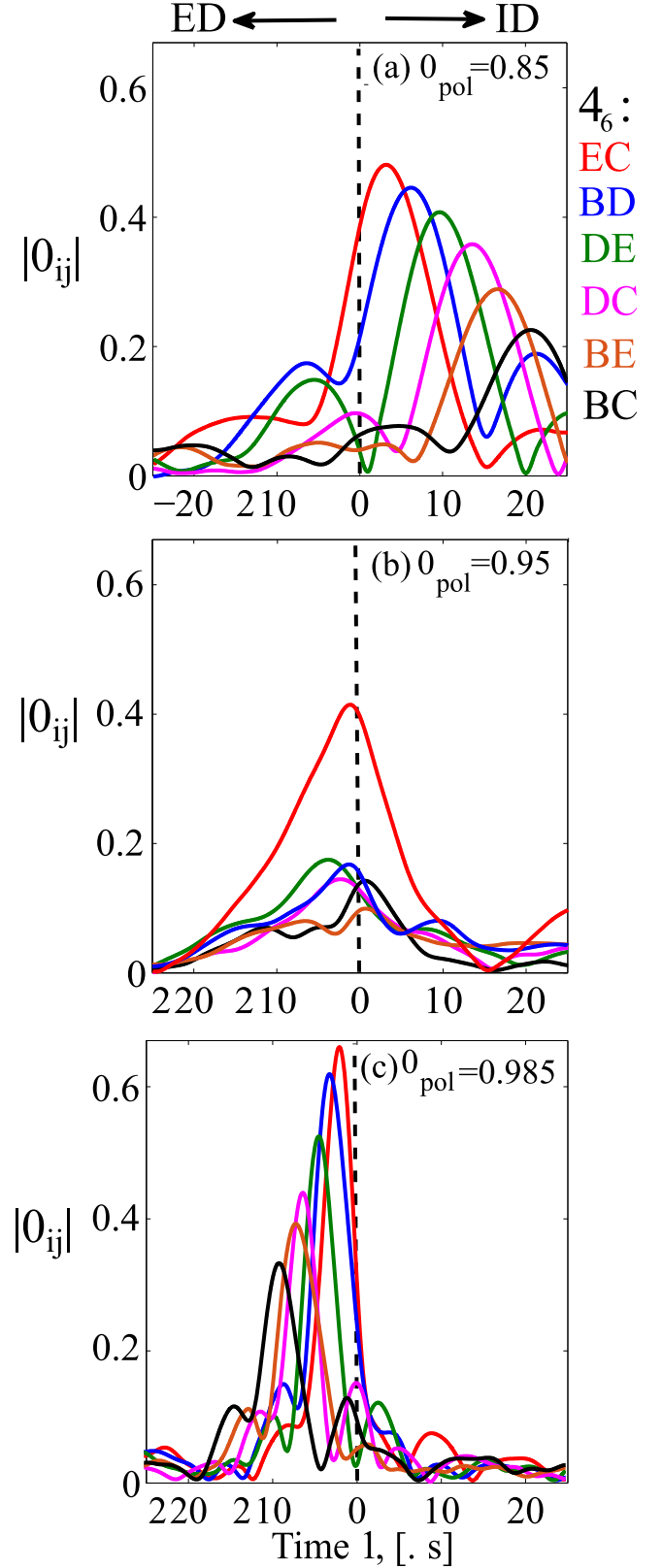

Figure 5. The cross-correlation functions (a) in the outer core, (b) in the pedestal, and (c) in the E_r well region of the L-mode plasma of #31 427.

$\rho_{pol} = 1.0$. The fluctuation level at $\rho_{pol} = 1$ can be used only as lower limit since reflectometry in the edge is most likely operating in the nonlinear regime where multiple scattering

processes can occur. The position of the maximum $\delta n_e/n_e$ is located around the maximum of the density gradient. This is consistent with the mixing length model which predicts $\delta n_e/n_e \approx k_r^{-1}|\nabla \log(n)|$, where k_r is the characteristic radial wavenumber of the turbulent density fluctuations. The measurement is shown for the antenna B, however, similar curves are obtained for all antennas.

Figure 4(b) shows the maximum correlation coefficient $\rho_m(\varepsilon_\perp) = \max_\tau(\rho(\varepsilon_\perp, \tau))$ as a function of radius for the different antenna combinations $EC(\varepsilon_\perp \approx 8\,\mathrm{mm})$, $DE(\varepsilon_\perp \approx 24\,\mathrm{mm})$ and $BC(\varepsilon_\perp \approx 45\,\mathrm{mm})$. It is important to note that at the density pedestal position $\rho_{\mathrm{pol}} = 0.925$–$0.98$ (see figure 4(e)) the correlation coefficient for large separations ($\varepsilon_\perp \approx 24$ and $45\,\mathrm{mm}$) falls to the noise level (dotted line), however, at short separations ($\varepsilon_\perp \approx 8\,\mathrm{mm}$) it remains at a measurable level. An examples of all possible CCFs for 3 different radial positions ($\rho_{\mathrm{pol}} = 0.85$, 0.95 and 0.985) are shown in figure 5. The maximum correlation time delays τ_m have different signs at $\rho_{\mathrm{pol}} = 0.85$ and 0.985 related to the fact that turbulence propagates in opposite directions.

The corresponded perpendicular velocity profile shown in figure 4(d) (blue line) is obtained from the maximum correlation time delay τ_m analyses (see figure 4(c)) using the equation

$$v_\perp = \frac{\varepsilon_\perp}{\tau_m(\varepsilon_\perp)}\left(1 - \frac{\tau_a^2}{\tau_d^2}\right), \tag{8}$$

where the correction parameter τ_a^2/τ_d^2 takes into account the distortion of the eddies during propagation. The error bars in $v_\perp$ are calculated from all possible combinations using a Bayesian probability approach [11]. Overlaid (green line) is the velocity profile from V-band Doppler reflectometry [30, 31] measured at 2.5 s. The measured $v_\perp$ is directed in electron diamagnetic (ED) direction in the plasma edge ($0.985 < \rho_{\mathrm{pol}} < 1$), while it changes sign to the ion diamagnetic direction (ID) in the outer core ($0.7 < \rho_{\mathrm{pol}} < 0.95$) due to the contribution of an intrinsic toroidal velocity. The measured $v_\perp = v_{E\times B} + v_{\mathrm{ph}}$ consists of both the background $E \times B$ drift and the intrinsic phase velocity of the turbulence, however, in case of AUG L-modes plasma $v_{E\times B}$ is dominant as demonstrated in several works for outer core [11, 32, 33] and edge [34, 35].

Note that although the maximum correlation level for $\varepsilon_\perp = 8\,\mathrm{mm}$ around the pedestal top ($0.925 < \rho_{\mathrm{pol}} < 0.98$) is still above the noise level, unfortunately, the velocity cannot be reconstructed here because the measured maximum correlation time delays are generally close to zero (figure 4(c)). According to equation (5) this implies either an infinite velocity (which is not realistic) or a very short dissipation time when $\tau_a/\tau_d \approx 1$. In other words, the density fluctuations dissipate energy (mutate) faster than they propagate. A significant correlation is observed only for combinations, where the separation smaller or comparable to the effective correlation length (i.e. for short separation $\varepsilon_\perp \approx 8\,\mathrm{mm}$). A loss of correlation at higher separation ($> 8\,\mathrm{mm}$) may be due to a combination of several factors: (i) small $v_\perp < \varepsilon_\perp/\tau_d$ allowing density fluctuations to decorrelate during their propagation, (ii) a decrease in the dissipation time τ_d or (iii) insufficient radial resolution of the diagnostic where rotation in different directions is averaged. This issue is discussed further in the next section.

3. The dissipation time measurements

τ_d can be determined from the decay of the CCF envelope, $\rho_{\mathrm{env}}(\tau_d) = \rho_{\mathrm{env}}(0)/e$, as indicated in figure 3(b) (black line). In practice, instead of fitting an envelope function, it is easier to fit through the maximum correlation time delays τ_m. In figure 6 the peak correlation level ρ_m is plotted as a function of the peak correlation time delay τ_m from different antenna combinations for two radial positions $\rho_{\mathrm{pol}} = 0.75$ and 0.99. The exponential fit $\rho_m(\tau_m) = \rho_0 \exp(-\tau_m^2/\tau_{dm}^2)$ (blue and red curves) permits one to estimate a τ_{dm}, which is only slightly smaller than the real τ_d (dashed curve)

$$\tau_{dm}^2 = \tau_d^2 - \tau_a^2, \tag{9}$$

because $\tau_a/\tau_d \approx 0.2 - 0.25$ (excluding the correlation loss region). In the following analyses it is assumed that $\tau_{dm} \approx \tau_d$ in the outer core ($0.6 < \rho_{\mathrm{pol}} < 0.9$) and in the E_r well ($\rho_{\mathrm{pol}} \approx 0.99$) regions. In figure 6 one can see that the dissipation time at $\rho_{\mathrm{pol}} = 0.75$ (red curve) is longer than at $\rho_{\mathrm{pol}} = 0.99$ (blue curve). This observation is discussed below.

3.1. Radial τ_d profiles and explanation for measured correlation loss

The radial profile of the dissipation time τ_d measured with the PCR in an Ohmic heated plasma is shown in figure 7(a) (black points). Here a frequency scan was performed at constant plasma density to obtain the radial profile. The plasma parameters for this discharge are: $n_{e0} = 2.52 \times 10^{19}\,\mathrm{m}^{-3}$, $B_{T0} = -2.5\,\mathrm{T}$ and $I_p = 0.6\,\mathrm{MA}$. The dissipation time increases from the edge ($0.98 < \rho_{\mathrm{pol}} < 1$) with $\tau_d \approx 5$–$10\,\mu\mathrm{s}$ to the outer core ($0.6 < \rho_{\mathrm{pol}} < 0.9$) with $\tau_d \approx 25$–$50\,\mu\mathrm{s}$. The increase of τ_d towards the outer core is observed in many Ohmic discharges. The corresponding velocity profile is shown in figure 7(b). Here, the yellow frame indicates the region where correlation is lost for all separations above $\varepsilon_\perp > 8\,\mathrm{mm}$ (see figure 4(b)) and, therefore, the velocity cannot be calculated with the PCR.

In figure 7(a) the measured τ_d (black points) is compared to the autocorrelation time τ_a (red points). As expected the dissipation time is longer than the autocorrelatton time, $\tau_d/\tau_a \approx 4$–5, but only in the outer core ($\rho_{\mathrm{pol}} < 0.9$) and in the E_r well ($\rho_{\mathrm{pol}} \approx 0.99$) regions. Hence, the autocorrelation time in these regions can be approximated by the propagation time $\tau_a \approx l_{\perp,\mathrm{eff}}/v_\perp$ (see equation (4)).

Figure 8(a) shows a zoom of the edge region. Figure 8(b) shows the corresponding velocity profile measured by PCR and DR for the same discharge as above. In the E_r well ($\rho_{\mathrm{pol}} \approx 0.99$) the autocorrelation time is dominated by the propagation time $\tau_a \approx l_{\perp,\mathrm{eff}}/v_\perp < \tau_d$ (see equation (4)). The autocorrelation time increases further inside the negative $v_\perp$ shear region due to a decrease in $v_\perp$. Simultaneously, there is a decrease of the dissipation time. It appears that around the point where $\tau_d \approx \tau_a$, i.e. at $\rho_{\mathrm{pol}} \approx 0.985$ for this discharge, the correlation for separations $\varepsilon_\perp > 8\,\mathrm{mm}$ is lost (see figure 4(b)) and stays below the noise level up to $\rho_{\mathrm{pol}} \approx 0.925$. The autocorrelation time in the correlation loss region $0.925 < \rho_{\mathrm{pol}} < 0.985$ (which still can be measured) does not increase further, but stays approximately constant
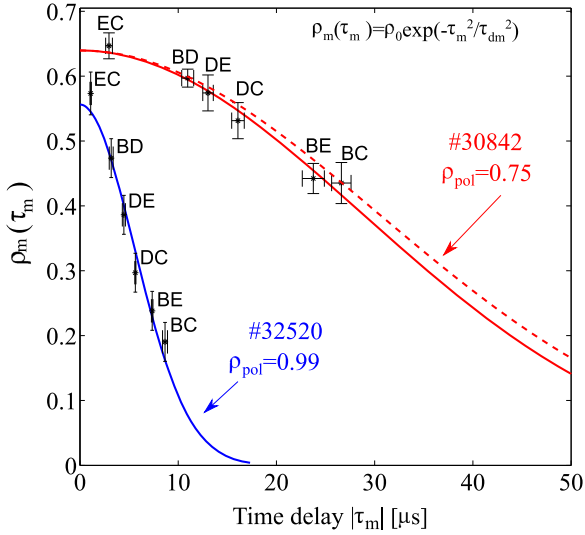
Figure 6. The fit (solid lines) through the peaks of CCFs $\rho_m(\tau_m)$ (points) for the outer core and the edge of AUG. Dashed line is the estimate of the envelope. Eddies in the outer core live longer than in the edge.
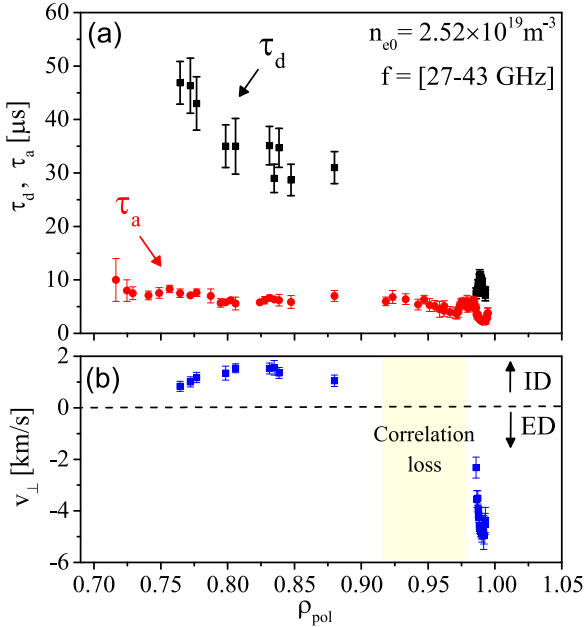

Figure 7. (a) The radial dissipation time τ_d and autocorrelation time τ_a profiles from discharge #32 481. (b) Corresponding velocity profile.

because it is dominated by the dissipation time $\tau_a \approx \tau_d$. This indicates that the dissipation time in pedestal region is reduced compared to the E_r well region.

The loss of correlation can be explained by the fact that the density fluctuations decorrelate faster than they propagate. Note that the zero time delay τ_m in figure 4(c) supports such an interpretation since, according to equation (5), this can only occur if $\tau_a \approx \tau_d$.

3.2. Comparison with theoretical predictions

There are several possible reasons for the increase of the dissipation time in the outer core ($\rho_{pol} < 0.9$) and its decrease
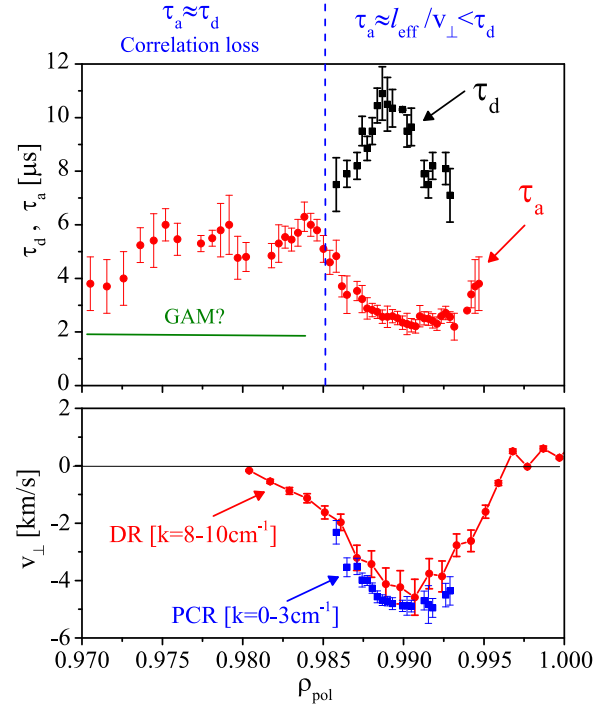

Figure 8. (a) The radial dissipation time τ_d and autocorrelation time τ_a profiles in the edge region of #32 481. (b) Velocity profile measured with PCR (blue) and DR (red).

around the pedestal region ($0.925 < \rho_{pol} < 0.98$). For fluid turbulence, Xin Zhao analytically calculated τ_d using a quasi-normal assumption of the Navier–Stokes equation taking into account a shear flow [36], where he obtained a dissipation time given by

$$\tau_d^{-2} = \frac{1}{l^2} \int_0^\infty (\delta v(k))^2 dk + \left(\frac{\partial v}{\partial r}\right)^2. \tag{10}$$

The equation indicates that τ_d depends on both the mean turbulent kinetic energy E and the velocity shear $\partial v/\partial r$. The value of τ_d in the case of plasma turbulence has been discussed by Terry [37] where the dissipation time in a plasma, without shear, is given by the turnover time of turbulent eddies,

$$\tau_d^{-1} = \tau_t^{-1} = \frac{\delta v}{l_r} = \frac{1}{l_r l_\theta} \frac{\delta \phi}{B}. \tag{11}$$

Here, δv and $\delta \phi$ are the rms fluid velocity and electric potential fluctuation level, respectively. Equation (11) qualitatively agrees with the first term of equation (10), where higher potential fluctuations mean a higher turbulent kinetic energy. In the strong shear environment, Terry further suggests that the dissipation time changes to coincide with the shear strain time

$$\tau_d^{-1} = \tau_s^{-1} = \frac{l_r}{l_\perp} \frac{\partial v}{\partial r}. \tag{12}$$

Using equations (10)–(12) we can suggest that:

(i) The increase of the dissipation time in the outer core (figure 7) may be due to an increase of the turnover time ($\tau_d \approx \tau_t$) caused by a reduction of the electric potential
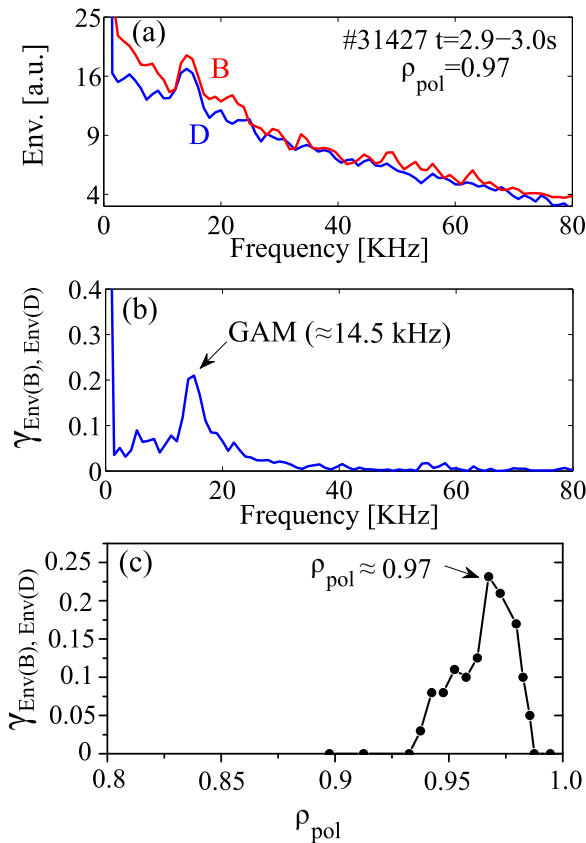
Figure 9. (a) The spectrum of the envelope for antennas B and D. (b) Coherence between the envelops from antennas B and D. (c) Radial dependence of GAM coherence amplitude measured with the PCR.

fluctuation amplitude. The contribution of the shear strain time in the outer core is small.

(ii) The decrease of the dissipation time in the velocity shear layer (figure 8) may be due to the decrease of the shear strain time ($\tau_d \approx \tau_s$). Using the maximum of the measured shear strain time we obtain $\max(\tau_s) = \max(\partial v_\perp / \partial r)^{-1} \approx 6 \, \mu s$, which is not too far from the measured values.

The reduction in τ_d around pedestal position together with small value of velocity in this region may explain the correlation loss. Nevertheless, the radial width of τ_d reduction region seems to be wider than can be explained by small shear strain time of mean flows only. A further candidate that may contribute to a decrease of τ_d around the pedestal region is the geodesic acoustic mode (GAM), which is also observed in a similar region using the PCR diagnostic [23]. The analyses here uses the observation that the envelope of high frequency density fluctuations are modulated by the GAM, as proposed by Nagashima [38]. The envelope is given by Env $(t) = \sqrt{x(t)^2 + H(x(t))^2}$, where $x(t)$ is the high frequency (250–450 kHz) real component of the complex signal and $H(x(t))$ its Hilbert transform. The GAM frequency can be seen in the spectrum of the envelope (figure 9(a)). Note, that the envelope shows only a small peak around 14.5 kHz. However, the coherence between envelopes from two different antennas (B and D) shows clearly the GAM frequency (figure 9(b)). The

GAM frequency has been compared earlier [23] to flow modulations measured by Doppler reflectometry and both diagnostics have measured GAMs oscillations with zero cross-phase. For the presented discharge we observe GAMs in PCR radial region $0.94 < \rho_{pol} < 0.98$ with its maximum amplitude around $\rho_{pol} \approx 0.97$ (figure 9(c)). Note that the DR observes the GAM in a narrower region [39] than PCR. This may be due to a lower resolution of the PCR diagnostic. The shear strain mechanism due to GAMs may additionally decrease the dissipation time of density fluctuations and contribute to the loss of correlation.

Note, however, that GAMs cannot contribute to the loss of correlation in the outer shear layer, $\rho_{pol} > 1$, (which we also observe in figure 4(b)) due to its absence in this region. Hence, the mean shear flow is the only possible candidate for decorrelation in the outer positive shear layer.

3.3. Dependence of measured τ_d on plasma parameters

The dependence of τ_d on the mean plasma parameters has been investigated with a database of 12 discharges analysed at multiple radial positions. Across the database, the mean local plasma parameters, such as the electron temperature T_e, magnetic field B_T, electron density n_e, density gradient length L_n, the perpendicular velocity $v_\perp$ and safety factor q_{95} are varied. Only Ohmic and electron cyclotron resonance heating was applied in these discharges. Figures 10(a)–(f) shows the dependence of τ_d on the above parameters in the outer core region, $0.6 < \rho_{pol} < 0.9$. To check for possible diagnostic influence the probing frequency and radial position are also plotted in figure 10(g) and (h). A regression analysis has been applied to the varying data sets which permits fitting of power law dependencies of τ_d. R^2_{adj} gives the variation in percent which can be explained by the power law dependencies [40].

τ_d shows a low correlation ($<25\%$) with magnetic field, density gradient length, safety factor, probing frequency f and radial position (see figures 10(b), (d), (f)–(h)). A small correlation is found with electron temperature $\tau_d \propto T_e^{-0.7 \pm 0.2}$ ($\approx 34\%$) and density $\tau_d \propto n_e^{-0.5 \pm 0.15}$ ($\approx 27\%$). A very high correlation ($\approx 74\%$) is found with the perpendicular velocity, $\tau_d \propto v_\perp^{-0.91 \pm 0.066}$. The dependence of τ_d on velocity is clearly visible not only in log–log scale, but also in linear scale (red points in figure 11), where we find $\tau_d \approx 40/v_\perp$ (here τ_d is in μs and $v_\perp$ in km s^{-1}). Note, however, that the spread of the points is higher, than can be explained by measured error bars only.

At the E_r well position, where a shear flow is also small, a correlation of τ_d with velocity as $\tau_d \approx 40/v_\perp$ is also observed (blue triangles in figure 11). Note that the direction of rotation in the edge (ED direction) is opposite to the outer core rotation (ID direction). The edge velocity in the E_r well region of Ohmic plasmas is usually higher compared to that in the outer core which may explain why τ_d in the edge is lower compared to the outer core.

According to equations (10) and (11) theory predicts a dependence of τ_d on the fluctuation velocity $1/\delta v_\perp$, but not on the mean velocity. Therefore the $\tau_d \propto 1/v_\perp$ dependence is not clear. One can speculate that there may be some correlation between δv and $v_\perp$ for the presented database. In this case one would need $\delta v / v_\perp \approx 20\%$ to explain the observations.
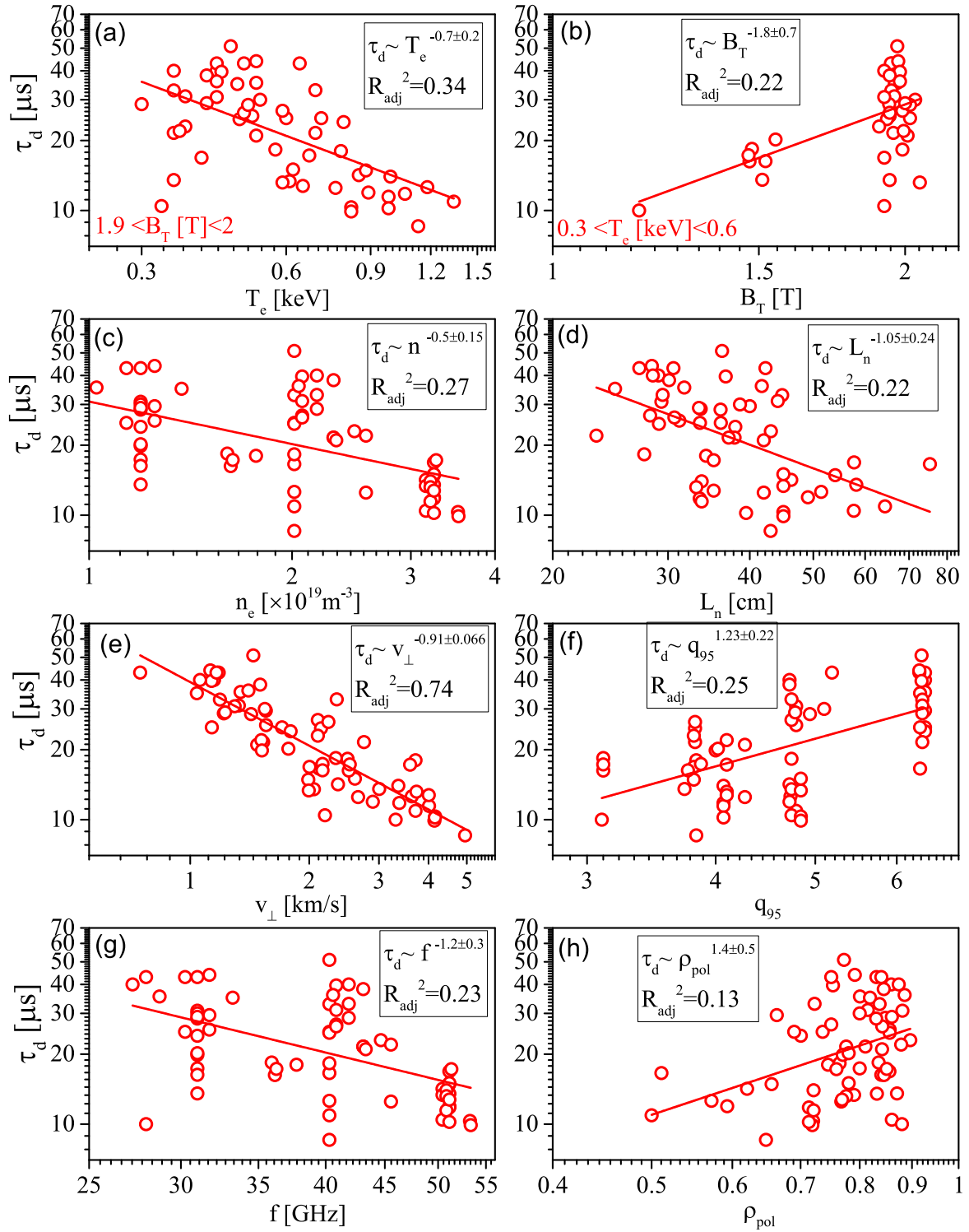
Figure 10. The dependence of dissipation time in the outer core region $0.6 < \rho_{pol} < 0.9$ on (a) electron temperature, (b) magnetic field, (c) local density, (d) density scale length, (e) perpendicular velocity, (f) safety factor, (g) probing frequency and (h) radial position.

4. The effective perpendicular correlation length measurements

$l_{\perp,eff}$ can be measured using two different methods. $l_{\perp,eff}$ can be obtained from measurements of correlation at zero time delay as function of the perpendicular separation

$\rho(\varepsilon_\perp, 0) = \rho_0 \exp(-\varepsilon_\perp^2 / l_{\perp,eff}^2)$ (see equation (3)). The minimal separation between reflection volumes of the PCR is around $\varepsilon_\perp \approx 0.7$–1.1 cm depending on radial position and the magnetic field pitch angle. Therefore, a measurement of $l_{\perp,eff}$ smaller than ≈ 1 cm is difficult with such an approach. Already the shortest combination in figure 3(b) shows a reduced correlation

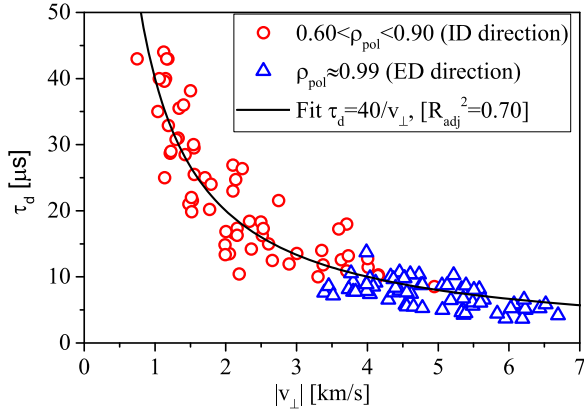**Figure 11.** Dependence of the dissipation time on the velocity in the outer core, $0.6 < \rho_{pol} < 0.9$ (red), and the E_r well, $\rho_{pol} \approx 0.99$ (blue). The sign of the velocity in the edge (electron diamagnetic) is opposite to that in the outer core (ion diamagnetic).
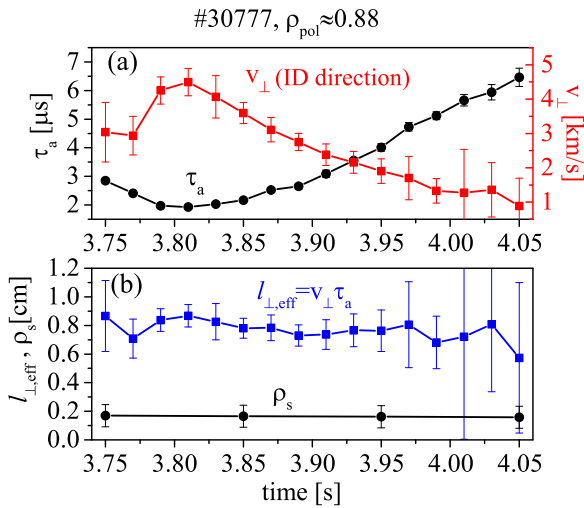

Figure 12. (a) Measured autocorrelation time (black) and perpendicular velocity (red). (b) Estimated effective correlation length using relationship $l_{\perp,eff} = v_\perp \tau_a$. $\rho_s = \sqrt{T_e m_i}/eB$ (black) is the drift wave length.

coefficient at zero time delay, and for other combinations it is comparable with the noise level. Fitting a Gaussian function with only a single $\varepsilon_\perp$ separation produces large error bars.

Alternatively, in the region where the turbulence propagates faster than it dissipate (i.e. when $\tau_a/\tau_d \ll 1$, see figure 7) the effective perpendicular correlation length can be obtained using the relationship $l_{\perp,eff} = v_\perp \tau_a$ (see equation (4)) as shown in figure 12 for the discharge #30 777. The analysed time period is not stationary and the velocity (red line) changes over time at a fixed position. The autocorrelation time (black line) also changes over time, however, the effective correlation length $l_{\perp,eff} = v_\perp \tau_a$ (blue line) stays nearly constant. Here, the error bars of $l_{\perp,eff}$ have been estimated from both uncertainty in $v_\perp$ and in τ_a. The value of $l_{\perp,eff}$ obtained using $v_\perp \tau_a$ is comparable to that from the space-correlation method, but the error bars are smaller.

4.1. Radial $l_{\perp,eff}$ profile

Profiles of the effective perpendicular correlation length $l_{\perp,eff}$ measured with the PCR at two different densities, $n_{e0} = 1.35$ and 2.5×10^{19} m^{-3}, from discharge #32 841, are shown in figure 13 (black points). A frequency scan has been performed to obtain the $l_{\perp,eff}$ profiles. At low density (figure 13(a)) $l_{\perp,eff}$ is of order of 1 cm and it increases only slightly towards the outer core over the region $\rho_{pol} = 0.6$–0.85. The edge region ($\rho_{pol} > 0.9$) is not covered in this example because the density was too low for the range of probing frequencies. The measurements at higher density (figure 13(b)) show slightly smaller values in the outer core ($\rho_{pol} < 0.9$), however, $l_{\perp,eff}$ is seen to increase in the E_r well region ($\rho_{pol} \approx 0.99$). This is observed in several Ohmic discharges for similar densities. One possible interpretation for the increased values of $l_{\perp,eff}$ could be the stretching of turbulent eddies along the direction of the sheared $E \times B$ flow (the velocity profile from this discharge is shown in figure 8(b)). Note that the wavenumber sensitivity also becomes smaller in the edge (see results using the Born approximation in section 5), but this is not enough to explain increase in $l_{\perp,eff}$. The values of $l_{\perp,eff}$ are compared with the local drift wave scale $\rho_s = \sqrt{T_e m_i}/eB$ (red line). The effective correlation length in the outer core is $l_{\perp,eff} \approx 5\rho_s$ while in the edge it is higher ($\approx 13\rho_s$).

4.2. Dependence of measured $l_{\perp,eff}$ on plasma parameters

The dependence of $l_{\perp,eff}$ on the mean plasma parameters has also been investigated using the same data set of 12 discharges as for the τ_d analyses. Figure 14 shows the dependence of $l_{\perp,eff}$ on T_e, B_T, n_e, L_n, $v_\perp$, q_{95}, f and ρ_{pol}. The output of the regression analyses are coefficients of linear dependencies and adjusted R-squared R^2_{adj}.

$l_{\perp,eff}$ is found not to correlate ($<9\%$) with density n_e, density gradient length L_n or safety factor q_{95} (figures 14(c), (d) and (f)). A weak dependence (figure 14(e)) is found on the velocity $v_\perp$ ($\approx 25\%$), which may simply be a result of $l_{\perp,eff} = v_\perp \tau_a$. The dependence of $l_{\perp,eff}$ on probing frequency and radial position (figures 14(g) and (h)), which defines sensitivity of diagnostic is also weak ($<7\%$). However, a quiet high correlation is found with electron temperature (54%) and magnetic field (49%). $l_{\perp,eff}$ increases with T_e and decreases with B_T (figures 14(a) and (b)). This dependence might be attributed to a dependence on the drift wave scale $\rho_s = \sqrt{m_i T_e}/eB$ which is theoretically predicted as a scale factor of the turbulent eddies. When $l_{\perp,eff}$ is plotted against ρ_s (figure 15) a linear dependence is found with $l_{\perp,eff} \approx 5\rho_s$. Figure 15 includes different magnetic fields $1\,\text{T} < B_T < 2.2\,\text{T}$ and different temperatures $0.3\,\text{keV} < T_e < 1.5\,\text{keV}$. Note, however, that due to the wavenumber sensitivity of the diagnostic the correlation length may be overestimated and the proportionality coefficient between $l_\perp$ and ρ_s may be smaller. This is discussed in section 5.1.

The effective perpendicular correlation length was also studied in the E_r well region ($0.98 < \rho_{pol} < 0.99$). Usually $l_{\perp,eff}$ in the E_r well is longer than in the outer core (see
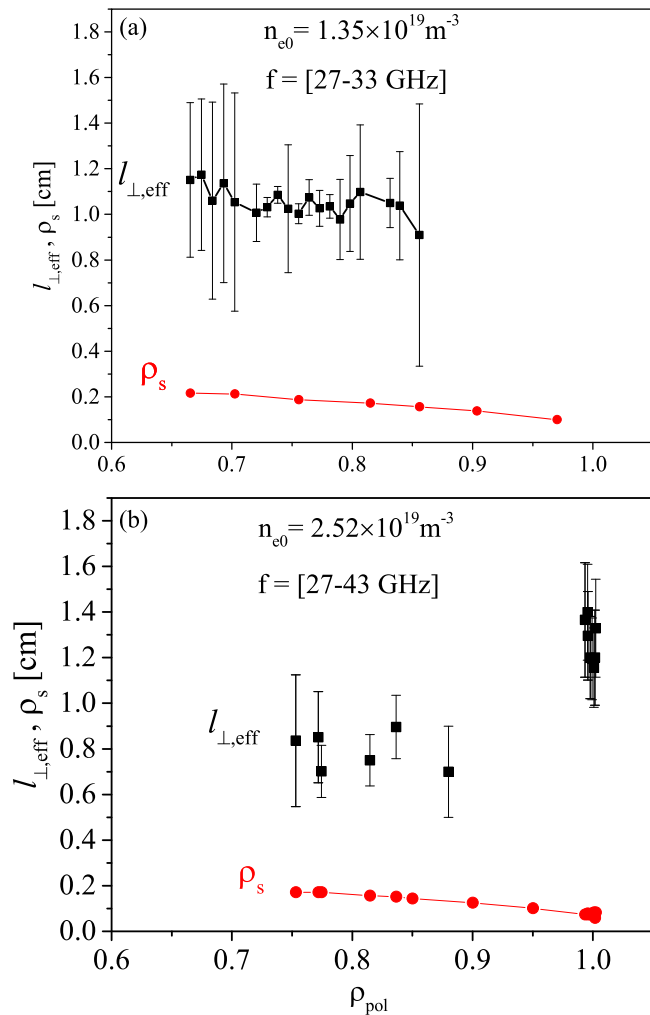
Figure 13. The profiles of effective correlation length for two different densities, $n_{e0} = 1.35$ (a) and 2.5×10^{19} m^{-3} (b). ρ_s (red) is the drift wave length.

figure 13(b)). However, here no clear dependence of $l_{\perp,\text{eff}}$ on physical parameters is found. The data are scattered and do not correlate with any parameter used.

4.3. Comparison to the radial correlation length

Using the additional radial correlation channel of the PCR diagnostic, the measured perpendicular and radial correlation lengths are compared. Figure 16(a) shows an example of the CCFs in radial correlation regime for four frequency separations ($\Delta f = 0$, 0.8, 1.6 and 2.4 GHz) from the antenna combination EC of discharge #32 437 ($I_P = 0.8$ MA, $B_T = -2.6$ T, $n_{e0} = 2.75 \times 10^{19}$ m^{-3}). The frequency of the fixed channel was $f_1 = 29.5$ GHz with a corresponding radial position $\rho_{\text{pol}} = 0.99$ (at the minimum of the E_r well). As expected, the maximal correlation coefficient ρ_m decays with the Δf (or radial separation) due to a finite radial correlation length. A non-zero time delay τ_m is also observed, which is a result of the finite perpendicular separation between the reflection points of antennas E and C ($\varepsilon_\perp \approx 8$ mm). A more detailed radial scan for all possible antenna combinations is

shown in figure 16(b). Here, 16 frequencies between 29.5 and 32.5 GHz with a frequency step of $\Delta f = 0.2$ GHz were used. The frequency difference Δf has been converted to radial separation ε_r using TORBEAM ray tracing code [41]. The radial correlation curve depends on the antenna combination (EC, DC and BC) due to different perpendicular separations between the antennas. The radial correlation length is estimated from the ρ_0/e level and amounts to $l_{r,\text{eff}} = 0.37 \pm 0.06$ cm. The same radial correlation length is obtained from all antenna combinations. A comparison to the drift wave scale at the E_r well position gives $l_{r,\text{eff}} \approx 4\rho_s$, which is smaller than $l_{\perp,\text{eff}} \approx 12\rho_s$. Thereby the ratio of perpendicular to radial correlation lengths is estimated at $l_{\perp,\text{eff}}/l_{r,\text{eff}} \approx 3$ (see blue points in figure 17). Such a high ratio may be a result of $E \times B$ shearing or different sensitivities of the diagnostic in the radial and perpendicular directions. The time delay τ_m in figure 16(c) is independent of the radial separation ε_r. This suggests that (i) the turbulent structures do not propagate significantly radially and (ii) the turbulent structures do not have a significant inclination in the radial-poloidal plane at the E_r well position, although such an inclination might be expected due to velocity shearing.

The same method has been applied to the outer core region ($\rho_{\text{pol}} \approx 0.78$) of discharge #34 928. The plasma parameters for this discharge are: $n_{e0} = 1.35 \times 10^{19}$ m^{-3}, $B_{T0} = -2.48$ T and $I_P = 0.8$ MA. During the discharge the electron temperature was varied by changing the electron cyclotron resonance heating power in 3 steps (0.0, 1.0 and 1.6 MW). Therefore, $l_{r,\text{eff}}$ and $l_{\perp,\text{eff}}$ can be compared for different values of the drift wave lengths $\rho_s \propto \sqrt{T_e}$ as shown in figure 17 (red points). The effective radial correlation length in the outer core is found to be $l_{r,\text{eff}} \approx 10\rho_s$, which is higher than in the E_r well. The perpendicular to radial correlation lengths ratio is estimated to be $l_{\perp,\text{eff}}/l_{r,\text{eff}} \approx 0.5$. This may be due to the natural anisotrophy of turbulent eddies or different sensitivity of the diagnostic in the poloidal and radial direction as discussed in section 5.1.

5. Assessment of diagnostic errors on $l_\perp$, l_r and τ_d measurements

It is important to investigate the influence of the microwave beam width (w_b) and beam curvature radius (r_b) on $l_{\perp,\text{eff}}$, $l_{r,\text{eff}}$ and τ_d measurements. In this section the weighting function (WF) approach is developed and applied to PCR measurements to investigate the response of the diagnostic. This approach is applicable only in the linear response regime of reflectometry when the density fluctuation level is less than several percent, i.e. in the outer core region of plasma ($\rho_{\text{pol}} < 0.9$, see figure 4(a)). The edge region ($\rho_{\text{pol}} > 0.95$) is in nonlinear regime of reflectometry [42], where the incident wave may experience multiple scattering processes and the interpretation of the signal is more challenging.

According to [43, 44], in the linear regime of reflectometry and O-mode polarization the complex signal of
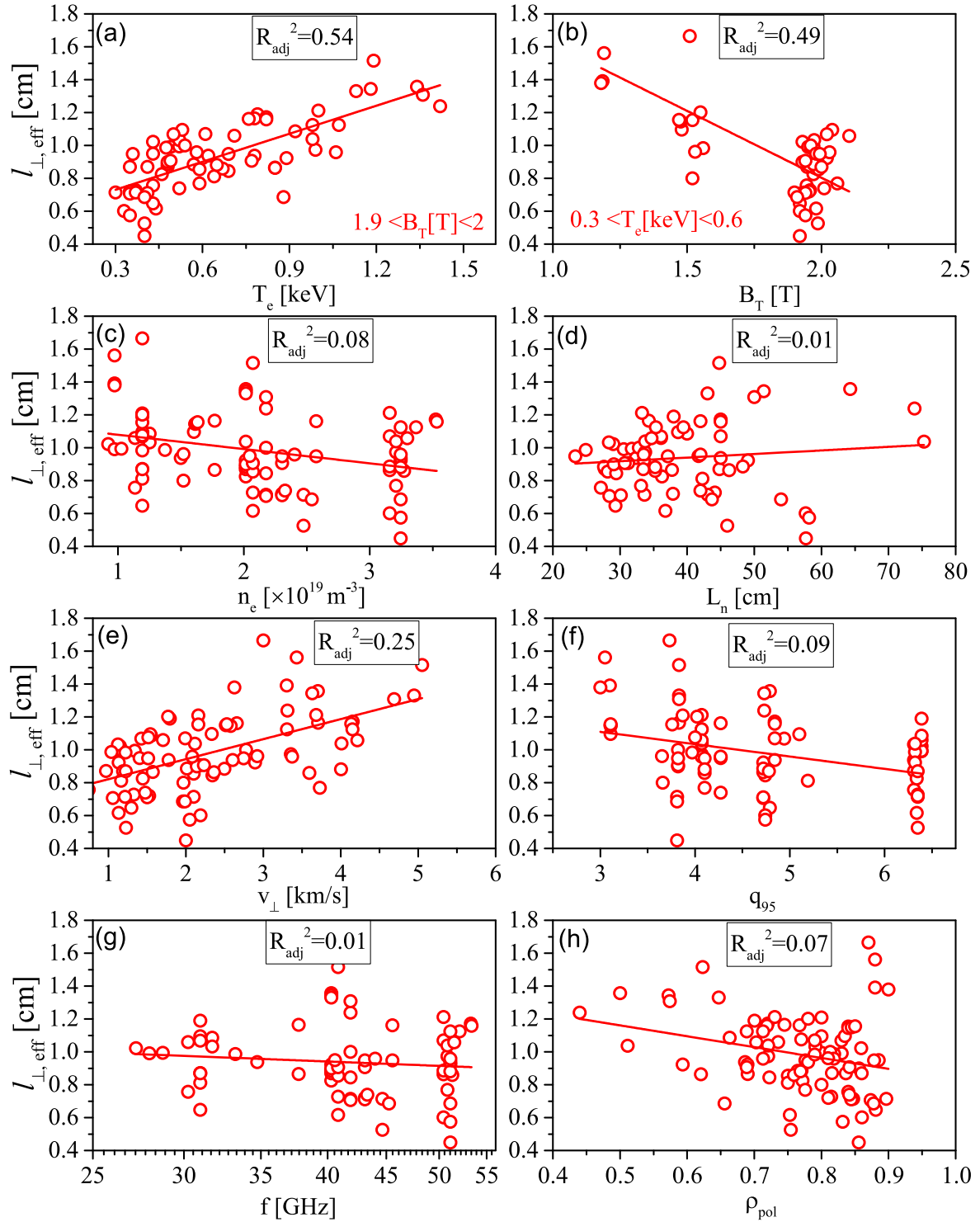
Figure 14. The dependence of effective perpendicular correlation length in the outer core region $0.6 < \rho_{pol} < 0.9$ on (a) electron temperature, (b) magnetic field, (c) density, (d) density scale length, (e) perpendicular velocity, (f) safety factor, (g) probing frequency and (h) radial position.

quadrature *IQ* detectors can be calculated as

$$I(t) + iQ(t) = C \int \frac{\delta n_e(\vec{r}, t)}{n_c(f)} W(\vec{r}) d\vec{r}, \quad (13)$$

where C is a dimensional factor and n_c the cut-off density.

The complex weighting function is defined as

$$W(\vec{r}) = W_I(\vec{r}) + iW_Q(\vec{r}) = \langle E_{Tx}(\vec{r}, t) E_{Rx}(\vec{r}, t) \rangle. \quad (14)$$

Here, $E_{Tx} = E_{Tx0}(\vec{r}) e^{i(\phi_{Tx}(\vec{r}) + \omega t)}$ is the (full-wave) electric field pattern of the transmitting antenna in the unperturbed plasma (i.e. the solution of the wave equation when density
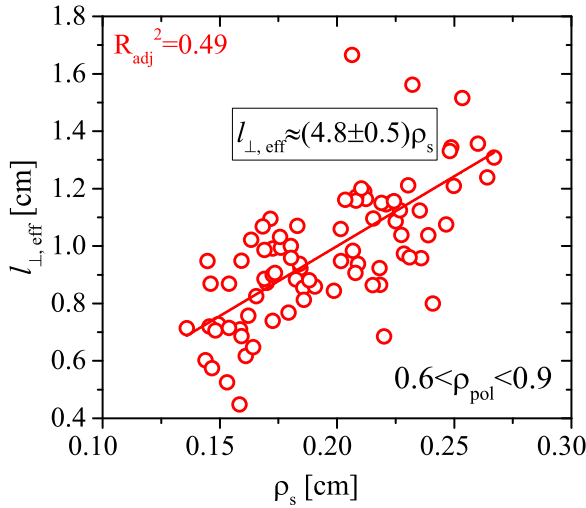
Figure 15. The dependence of effective correlation length on drift wave scale ρ_s in the outer core region $0.6 < \rho_{pol} < 0.9$.

fluctuations are neglected) and $E_{Rx} = E_{Rx0}(\vec{r})e^{i(\phi_{Rx}(\vec{r}) - \omega t)}$ is the fictitious field that would be excited by the receiving antenna if it was transmitting but is time inverted. The brackets denote averaging over a microwave period. A similar equation for the measured signal in the received antenna has been obtained by Hutchinson [45] using Green's function of the wave equation, but in 1D geometry. Equation (13) has been compared earlier with full-wave simulations [7, 29] and good agreement has been obtained for small density fluctuation levels.

For the geometry of the PCR on AUG the WF is calculated using a bistatic configuration, i.e. different transmitting and receiving antennas. The combinations Rad-B and Rad-C (see figure 1) are considered, however, any antenna pair combination can be used. The unperturbed full-wave distributions of the transmitting antenna, E_{Tx}, and the receiving antenna, E_{Rx}, are found with the code developed in [44] using a cylindrical coordinate system. In the analysis here, the AUG CLISTE equilibrium magnetic surfaces [46] are approximated by cylindrical surfaces and $n_e(r)$ is assumed to be independent of the poloidal angle (for more details, see [22]). The electric field distribution in the horn antenna mouth in the H-plane is given by

$$E(y) = E_0 \cos\left(\frac{\pi y}{2Y_a}\right) \exp\left\{ik_0 R_a \sqrt{1 + \frac{y^2}{R_a^2}}\right\}, \quad (15)$$

where y is coordinate along the H-plane (poloidal direction) of the antenna mouth. Here, the AUG half width of the antenna mouth $Y_a = 2.35\,cm$ and the length of the horn $R_a = 5.71\,cm$ are used. An example of the calculated real part of the WF $W_{IB}(r, \theta)$ for the in-phase signal $I(t)$ for discharge #32 841 is shown in figure 18. For this example, the $1/e\,E^2$ half beam width of transmitting antenna at the cut-off layer amounts to $w_b \approx 8.5\,cm$ and the beam curvature radius $r_b \approx 85\,cm$. The overlaid blue curve is the ray tracing
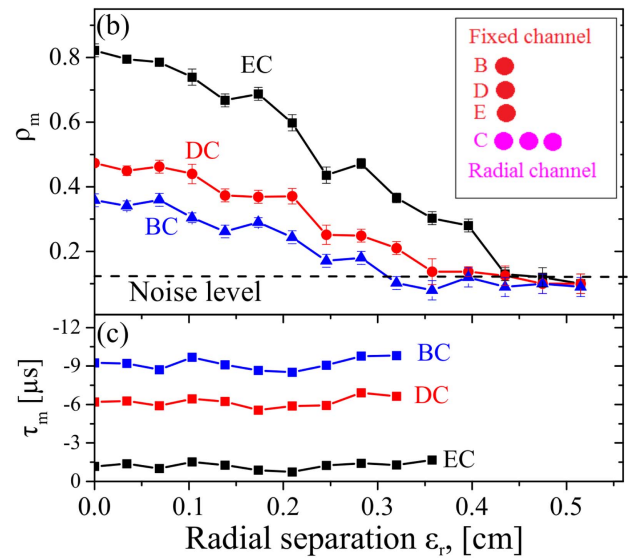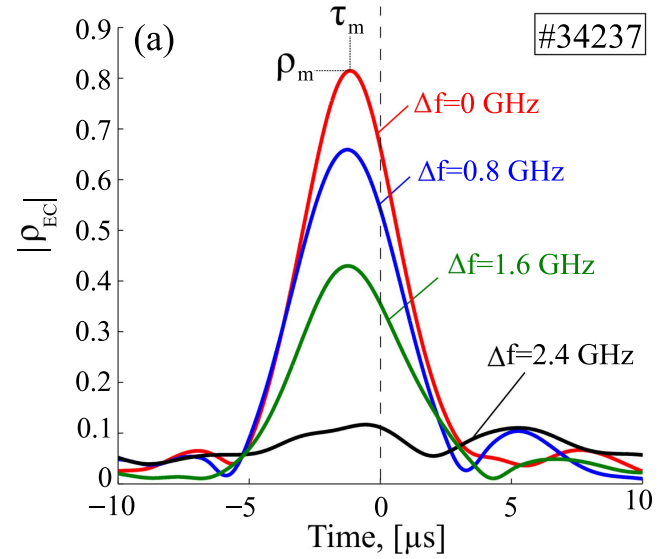

Figure 16. (a) CCFs as function of frequency difference Δf for antenna combination EC. (b) Maximum correlation coefficient as function of radial separation ε_r for all antenna combinations. (c) Corresponding time delays.

calculation from the TORBEAM code [41] for combination Rad-B. One can see that the reflection point of the ray tracing is close to the actual maximum of $W_{IB}(r, \theta)$. A similar WF is obtained for antenna combination Rad-C.

Using the computed WFs, in section 5.1 a synthetic CCFs between different antennas is calculated, while in section 5.2 a sensitivity function $S(k_\theta)$ of the PCR to different poloidal wavenumbers and radial positions is investigated.

5.1. Synthetic CCF

First, a synthetic CCF between different antennas in the presence of rotating density fluctuations is investigated. The density fluctuation pattern is assumed to have a Gaussian

shape in both the poloidal and radial directions

$$\delta n(r, \theta, t) = \sum_{k_r} \sum_m \exp\left(-\frac{k_r^2 l_r^2}{8} - \frac{m^2 l_\theta^2}{8r_c^2}\right)$$
$$\times \cos(k_r r + \psi_{k_r})\cos(m\theta + \omega_\theta t + \psi_m). \quad (16)$$

Here, l_r and l_θ are the radial and poloidal correlation lengths at the cut-off position (r_c), k_r the radial wavenumber, $m = k_\theta r$ the poloidal mode number and ψ_{k_r}, ψ_m a random phase of different turbulent modes. The density fluctuations rotate with a constant angular velocity $\omega_\theta = v_\theta/r$ along the cut-off layer in the poloidal direction. A snapshot of the δn fluctuations with $l_r = l_\theta = 1$ cm around the cut-off layer position (dotted line) is shown in figure 19(a). Note that such a model does not include the dissipation of turbulent eddies during propagation (i.e. $\tau_d = \infty$, frozen turbulence).

The synthetic signals of the *I* and *Q* detectors are calculated using equation (13), by taking the convolution of the density fluctuations $\delta n(r, \theta, t)$ with the WF $W_j(r, \theta)$, where index *j* denotes different receiving antennas (B and C). An example of the calculated ACF and CCF (ρ_{BB} and ρ_{BC}) of the synthetic signals is shown in figure 19(b). As expected, ρ_{BC} exhibits a time delay due to the propagation, which agrees with the input velocity. ρ_{BC} also shows a slightly reduced peak correlation (although the dissipation time of the density fluctuations is infinity). This can be explained by the different WFs $W_j(r, \theta)$ for antennas B and C. However, the reduction amounts to 1%–3% only, which is significantly smaller than in the experiment and thus can be neglected. This result suggests that the measured dissipation time in figure 3(b) is almost not influenced by the geometry of the beam.

The estimated effective perpendicular correlation length $l_{\perp,\text{eff}}$ of the PCR for different input correlation lengths $l_\theta = l_r$ is also investigated. As in the experiment, the effective correlation length is calculated using $l_{\perp,\text{eff}} = v_\perp \tau_a$, where τ_a is the autocorrelation time. Figures 20(a) and (b) shows a comparison of the simulated ACF ρ_{BB} (blue lines) with the ACF of the input density fluctuations $\rho_{\delta n \delta n}$ (black lines) for two poloidal correlation lengths, 0.25 and 3 cm. The time was multiplied by the poloidal velocity v_θ at the cut-off layer (the same for both cases). For the larger correlation length $l_\theta = 3$ cm a quiet good agreement is observed, however, for $l_\theta = 0.25$ cm the ACF is significantly wider compared to the original one of the density fluctuations. This can be explained as the influence of the wavenumber sensitivity of the PCR antenna as discussed in the next section. The dependence of the effective perpendicular correlation length $l_{\perp,\text{eff}}$ at $1/e$ level on the input poloidal correlation length l_θ is shown in figure 21 (blue points), from which it can be concluded that for the presented frequency and radial position:

(i) For $l_\theta > 0.4$ cm a roughly linear dependence of $l_{\perp,\text{eff}}$ on l_θ is observed.
(ii) For $l_\theta < 0.4$ cm $l_{\perp,\text{eff}}$ is strongly influenced by the diagnostic response.

The measured effective perpendicular correlation length in figure 15 (blue points) varies between 0.6 and 1.8 cm and
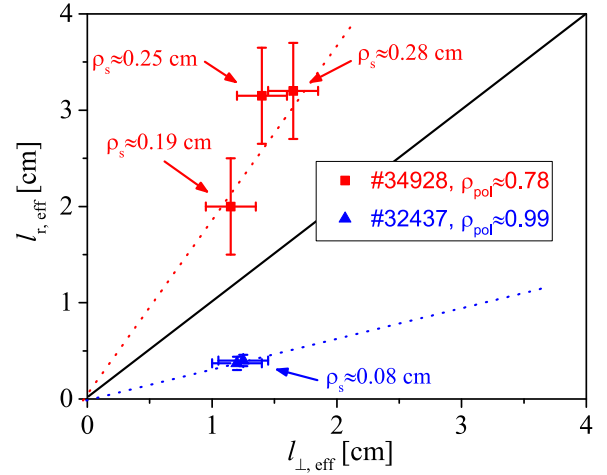

Figure 17. Comparison of the effective perpendicular correlation length to the radial one in the outer core (red) and in the E_r well position (blue).
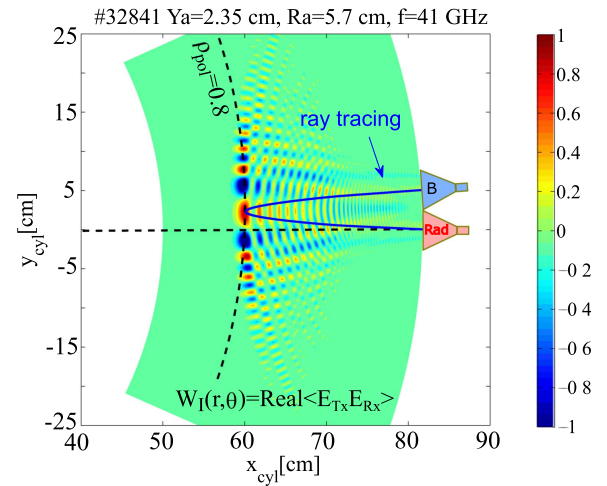

Figure 18. Calculation of real part of weight function $W_{IB} = \text{Re}\langle E_{\text{Tx}}(\vec{r}, t)E_{\text{Rx}}(\vec{r}, t)\rangle$ in cylindrical coordinates for the case of bistatic configuration.

therefore, can be overestimated by a factor of 1.4–2 due to the contribution of the beam size. However, since a linear dependence in figure 21 holds, the dependence on ρ_s may still be real, but with a smaller coefficient, $l_\perp \approx 3\rho_s$, instead of the measured $l_{\perp,\text{eff}} \approx 5\rho_s$.

The WF approach was also applied for the interpretation of measured radial correlation length $l_{r,\text{eff}}$, which is also found to be overestimated (red triangles in figure 21), but by a higher factor of 3–4. Figure 20(c) shows an example of comparison of the effective radial correlation length with that of the input density fluctuations. The overestimation of the radial correlation length is in agreement with results presented in [6, 7]. Therefore, the real radial correlation length is also about $l_r \approx 3\rho_s$. The difference in the measured radial and perpendicular correlation length is therefore probably a diagnostic effect.
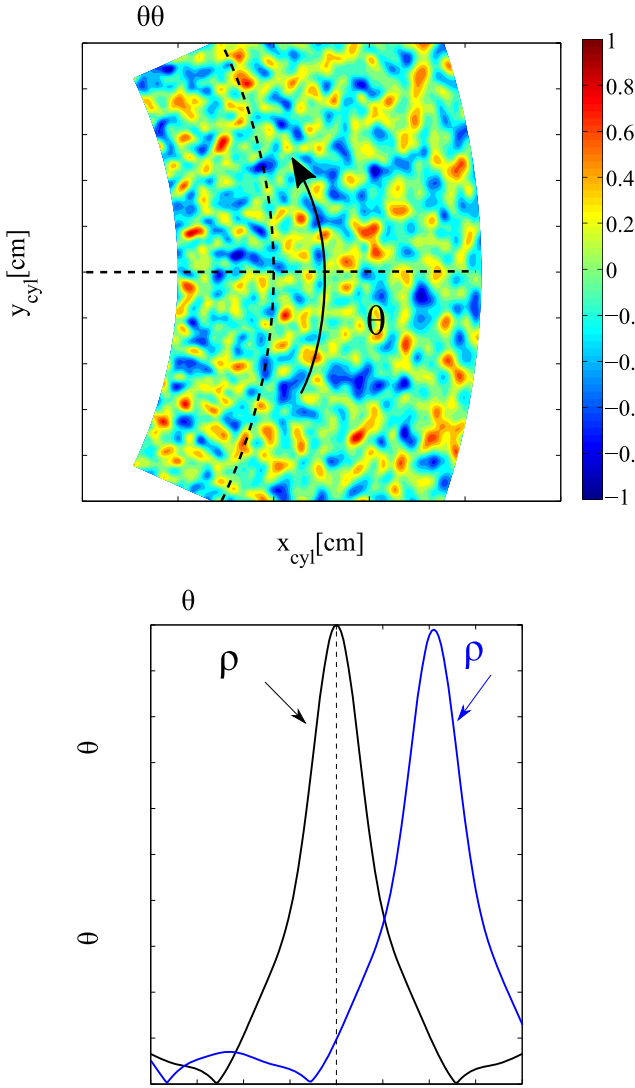
Figure 19. (a) Example of a synthetic density fluctuation snapshot used in the simulations. (b) The auto- (black) and cross- (blue) correlation functions of synthetic PCR signal.
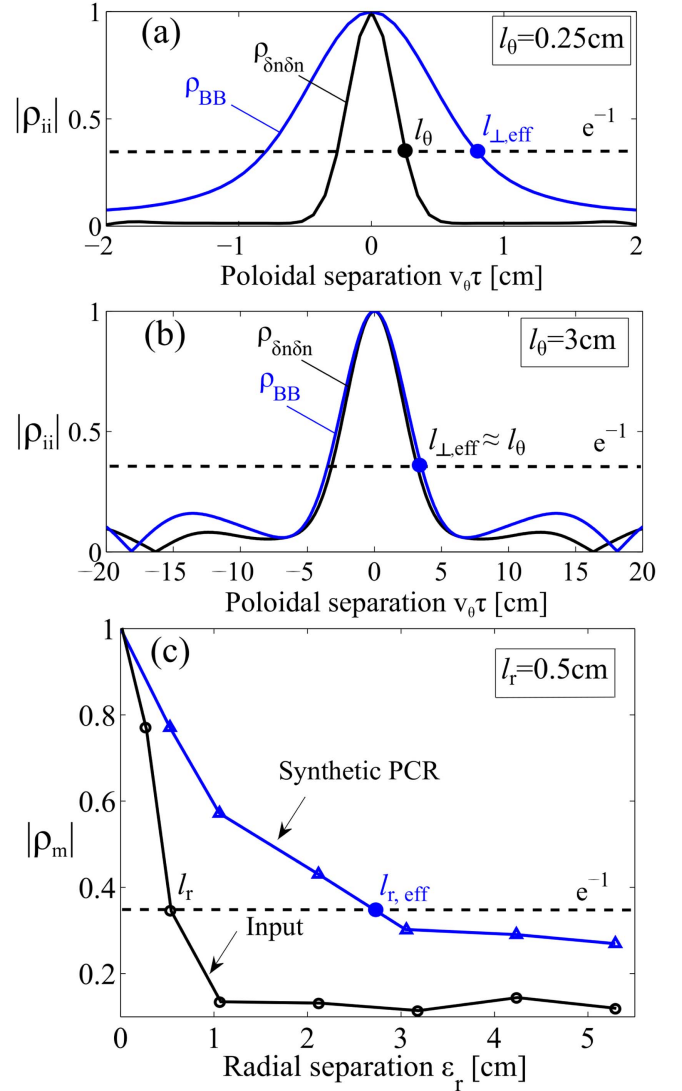

Figure 20. (a) and (b) Comparison of calculated autocorrelation function ρ_{BB} from synthetic signals with that of the input density fluctuations $\rho_{\delta n \delta n}$ for two poloidal correlation lengths (0.25 and 3 cm). Note that scales of the *x*-axes differ. (c) Comparison of the calculated radial correlation length with that of the input density fluctuations.

5.2. Sensitivity of the PCR to poloidal wavenumbers

The influence of the beam on the measured perpendicular correlation length can be explained by the sensitivity $S(k_\theta, r_0)$ of PCR to different poloidal wavenumbers. Here, $S(k_\theta, r_0) = \langle I^2(t) + Q^2(t) \rangle$ is the average response of *IQ* detectors (calculated using equation (13)) to the rotating harmonic density fluctuations localized at radius r_0

$$\delta n(r, \theta, t) = \cos(m\theta - \omega_\theta t)\exp\left(-\frac{(r - r_0)^2}{(\Delta r/2)^2}\right). \quad (17)$$

In this equation $m = k_\theta r_0$ is the poloidal mode number of the fluctuations, Δr the radial size and ω_θ the frequency of rotation. In some sense, the sensitivity function is the Fourier decomposition of the WF from figure 18. The example of the normalized $S(k_\theta, r_0)$ for the conditions of discharge #32 841 and frequency $f = 41$ GHz is shown in figure 22. The radial size of the fluctuations is set to be $\Delta r = 0.5$ cm. As expected, the system is most sensitive at the cut-off layer and its sensitivity decays with k_θ. The PCR diagnostic acts as a low pass filter in k_θ

space and this explains why the correlation length in figure 21 is overestimated. For the presented case the sensitivity width at the $1/e$ level is calculated to be $k_{\theta s} \approx 2.6\,\mathrm{cm}^{-1}$. This estimate is similar to the full-wave estimate from TEXTOR [47] with a similar antenna geometry. Note that the sensitivity is much better than can be explained by the beam width size due to influence of the beam curvature, as discussed below. We assume that the sensitivity to perpendicular wavenumbers is similar, i.e. $k_{\perp s} \approx k_{\theta s}$. The characteristic sensitivity length (or poloidal resolution of correlation length) can be roughly approximated as $l_s = 2/k_{\theta s}$. For the results from figure 22 this is approximately 0.77 cm, which agrees with the cross-correlation analyses in figure 21.

The dependence of the sensitivity $k_{\theta s}$ has been investigated as a function of radial position and frequency. Figure 23 shows the dependence of the calculated $k_{\theta s}$ on the radial
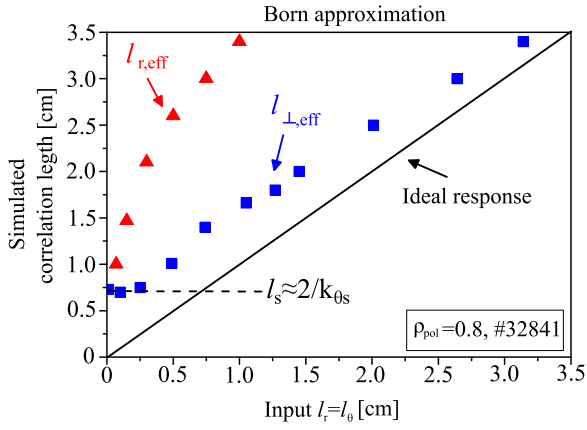
Figure 21. The effective correlation lengths, $l_{\perp,\text{eff}}$ and $l_{r,\text{eff}}$, from synthetic PCR signals versus correlation length of the input density fluctuation.
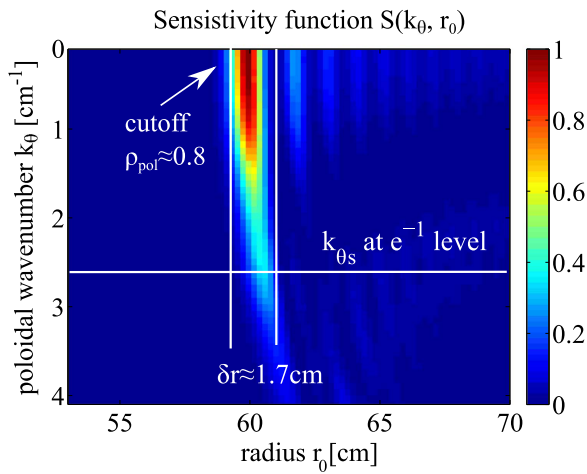

Figure 22. Sensitivity of the PCR $S(k_\theta, r_0)$ to different poloidal wavenumbers k_θ and radial positions r_0 in case of Born scattering approximation.

position for two different line average densities of $n_{e0} = 1.35$ and $2.5 \times 10^{19}\,\text{m}^{-3}$. The sensitivity improves towards the outer core, while at the fixed cut-off position it increases with frequency. The value of sensitivity at the $1/e$ level has been already discussed by Lin *et al* [48], based on a phase screen model (i.e. neglecting plasma propagation effects), where was shown that the sensitivity depends on the effective curvature radius $r_{\text{eff}} = r_c r_b / (r_c + r_b)$:

$$k_{\theta s}^2 = \frac{4}{w_b^2} + 4k_0^2 w_b^2 / r_{\text{eff}}^2. \tag{18}$$

Here, r_c is the cut-off curvature radius, r_b the beam curvature radius and w_b the $1/e\,E^2$ beam width. Note that in this equation a Gaussian distribution for the beam was assumed, which in general can differ from the horn antenna distribution. Similar dependencies have been obtained by Hirsch [49] and Bulanin [44]. In case of AUG PCR microwave beam, the sensitivity is dominated by the second term of equation (18), which may explain the improvement of the sensitivity in figure 23 towards outer core (because r_c is lower) and with frequency (because $k_0 = 2\pi f/c$ is higher).
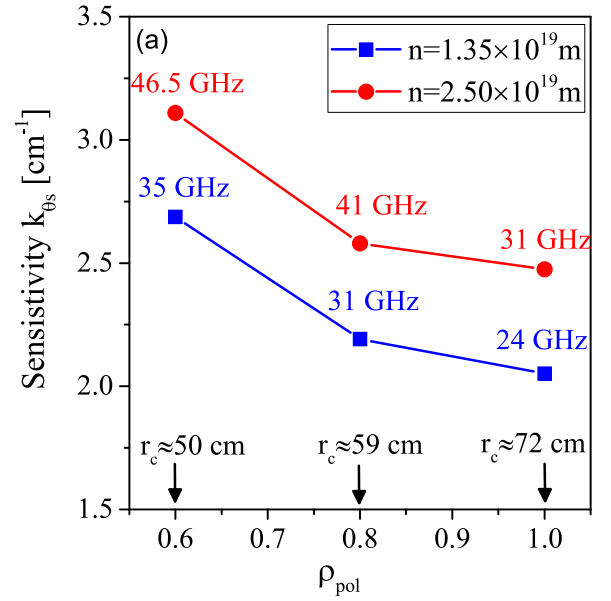

Figure 23. The sensitivity of diagnostic at $(1/e)$ level as function of frequency and radial position.

Note, however, that both the beam width w_b and phase front curvature r_b depend on the propagation of microwaves in the plasma (see e.g. [47]) and are not known *a priori*.

The decrease of sensitivity $k_{\theta s}$ towards the edge region, will influence the effective correlation length at the E_r well region and may explain $\approx 30\%$ of the increase of the effective correlation length observed in figure 13(b). Note, however, that in the edge ($\rho_{\text{pol}} > 0.95$) the diagnostic operates in the nonlinear response regime, where the presented analyses may not be applied. Therefore future investigations of the sensitivity function in the nonlinear response regime will be important for a correct interpretation of measurements in the edge.

6. Conclusion

In this work an O-mode PCR diagnostic with additional radial correlation channel was applied to the study of the correlation of turbulent density fluctuations. The dissipation time τ_d, the effective perpendicular correlation length $l_{\perp,\text{eff}}$ and the effective radial correlation length $l_{r,\text{eff}}$ were measured from the outer core to the edge in the L-mode plasmas of the AUG tokamak. The diagnostic operates in the linear response regime for $\rho_{\text{pol}} < 0.9$, while the regime successively transit to the nonlinear for $\rho_{\text{pol}} > 0.95$.

The typical dissipation time increases from the edge ($0.98 < \rho_{\text{pol}} < 1$) with $\tau_d \approx 5$–$10\,\mu\text{s}$ to the outer core ($0.6 < \rho_{\text{pol}} < 0.9$) with $\tau_d \approx 25$–$50\,\mu\text{s}$, which may be explained by an increase of the density fluctuation turnover time caused by a reduction of the electrical potential fluctuation amplitude (see equation (11)). Future measurements of electric potential fluctuations will be an important element to validate this interpretation. It was found that in the outer core region ($\rho_{\text{pol}} < 0.9$) τ_d correlates with the perpendicular velocity as $\tau_d \approx 40/v_\perp$ (τ_d is in μs and $v_\perp$ in $\text{km}\,\text{s}^{-1}$). It was further observed that τ_d additionally decreases in the pedestal

region ($\rho_{\rm pol} = 0.925$–0.98) leading to a loss of correlation between poloidally separated measuring points. This may be due to the influence of the mean $E \times B$ or GAM shear flows as suggested by equation (12). The small flow velocity in this region, when $v_\perp < \varepsilon_\perp / \tau_d$, or weak radial resolution of the PCR may also contribute to the loss of measured correlation.

The measured effective perpendicular correlation length varies from 0.6 to 1.8 cm. The dependence of $l_{\perp,\rm eff}$ on mean plasma parameters was studied. In the outer core ($\rho_{\rm pol} < 0.9$) $l_{\perp,\rm eff}$ correlates with the electron temperature T_e and magnetic field B_T such that $l_{\perp,\rm eff} \approx 5\rho_s \propto \sqrt{T_e}/B_T$, which is theoretically predicted to be the size scale of turbulent density fluctuations. In the edge region no correlation of $l_{\perp,\rm eff}$ with mean plasma parameters is found. However, $l_{\perp,\rm eff}$ in the E_r well region is longer than in the outer core. The effective perpendicular correlation length is compared to the radial one, where $l_{\perp,\rm eff}/l_{r,\rm eff} \approx 0.5$ is found in the outer core and $l_{\perp,\rm eff}/l_{r,\rm eff} \approx 3$ in the E_r well region.

Finally, the WF approach was applied to interpret the measurements. It was found that in the linear response regime the measured $l_{\perp,\rm eff}$ and $l_{r,\rm eff}$ may be overestimated by a factor of 1.4–2 and 3–4 due to the influence of the wavenumber sensitivity of the diagnostic. This implies that the real correlation length is smaller, $l_\perp \approx l_r \approx 3\rho_s$. It was also shown that the microwave beam size has little effect on the measured dissipation time.

The characterization of the structure of the density fluctuations in fusion plasmas from this work can be used as basis of a detailed comparison with turbulence simulation codes. This will help to test the physical models in these codes and to build more complete models for the associated radial transport. To include possible diagnostic effects, a synthetic PCR diagnostic (e.g. using the Born approximation) can be applied to simulated data in order to enable cross-comparisons of equivalent quantities. Future work will use the presented method to study changes in the correlation length and dissipation time during the low to high (L–H) confinement transitions.

ORCID iDs

D Prisiazhniuk ⬤ https://orcid.org/0000-0002-0249-8397
A Krämer-Flecken ⬤ https://orcid.org/0000-0003-4146-5085

References

[1] Nazikian R, Kramer G J and Valeo E 2001 A tutorial on the basic principles of microwave reflectometry applied to fluctuation measurements in fusion plasmas *Phys. Plasmas* **8** 1840

[2] Hornung G, Clairet F, Falchetto G L, Sabot R, Arnichand H and Vermare L 2013 Turbulence correlation properties measured with ultrafast sweeping reflectometry on Tore Supra *Plasma Phys. Control. Fusion* **55** 125013

[3] Rhodes T L, Leboeuf J N, Sydora R D, Groebner R J, Doyle E J, McKee G R, Peebles W A, Rettig C L, Zeng L and Wang G 2002 Comparison of turbulence measurements from DIII-D low-mode and high-performance plasmas to turbulence simulations and models *Rev. Sci. Instrum.* **63** 2141

[4] Kurzan B, de Pena Hempel S, Holzhauer E, Scott B, Serra F, Suttrop W, Zeiler A and the ASDEX Upgrade Team 2000 Measurement and scaling of the radial correlation lengths of turbulence at the plasma edge of ASDEX Upgrade *Plasma Phys. Control. Fusion* **42** 237

[5] Schrimer J, Conway G D, Holzhauer E, Suttrop E, Zohm H and the ASDEX Upgrade Team 2007 Radial correlation length measurements on ASDEX Upgrade using correlation Doppler reflectometry *Plasma Phys. Control. Fusion* **49** 1019

[6] Gusakov E Z and Yakovlev B O 2002 Two-dimensional linear theory of radial correlation reflectometry diagnostics *Plasma Phys. Control. Fusion* **44** 2525

[7] Leclert G, Heuraux S, Gusakov E Z, Popov A Y, Boucher I and Vermare L 2006 Full-wave test of the radial correlation reflectometry analytical theory in linear and nonlinear regimes *Plasma Phys. Control. Fusion* **48** 1389

[8] Ritz C P *et al* 1988 Advanced plasma fluctuation analysis techniques and their impact on fusion research *Rev. Sci. Instrum.* **59** 1739

[9] Mahdizadeh N, Greiner F, Happel T, Kendl A, Ramisch M, Scott B D and Stroth U 2007 Investigation of the parallel dynamics of drift-wave turbulence in toroidal plasmas *Plasma Phys. Control. Fusion* **49** 1005

[10] Birkenmeier G, Ramisch M, Fuchert G, Kohn A, Nold B and Stroth U 2013 Spatial structure of drift-wave turbulence and transport in a stellarator *Plasma Phys. Control. Fusion* **55** 015003

[11] Prisiazhniuk D, Krämer-Flecken A, Conway G D, Happel T, Lebschy A, Manz P, Nikolaeva V, Stroth U and the ASDEX Upgrade Team 2017 Magnetic field pitch angle and perpendicular velocity measurements from multi-point timedelay estimation of poloidal correlation reflectometry *Plasma Phys. Control. Fusion* **59** 025013

[12] Cripwell P, Costley A E and Fukuda T 1992 Correlation reflectometry measurements at JET *Proc. IAEA Tech. Com. Meeting (Abingdon, UK)* pp 168–76

[13] Conway G D, Vayakis G, Fessey J A and Bartlett D V 1999 A reflectometer for fluctuation and correlation studies on the Joint European Torus tokamak *Rev. Sci. Instrum.* **70** 1063

[14] Vershkov V A, Soldatov S V, Shelukhin D A and Chistiakov V V 2000 Experimental investigation of ion-temperature-gradient-like turbulence characteristics in T-10

core plasmas with toroidal and poloidal correlation reflectometry *Nucl. Fusion* **39** 1775

[15] Vershkov V A, Shelukhin D A, Soldatov S V, Urazbaev A O, Grashin S A, Eliseev L G, Melnikov A V and the T-10 team 2005 Summary of experimental core turbulence characteristics in Ohmic and electron cyclotron resonance heated discharges in T-10 tokamak plasmas *Nucl. Fusion* **45** S203–226

[16] Krämer-Flecken A, Dreval A, Soldatov S, Rogister A, Vershkov V and the TEXTOR-team 2004 Turbulence studies with means of reflectometry at TEXTOR *Nucl. Fusion* **44** 1143–57

[17] Krämer-Flecken A, Soldatov S, Vowinkel B and Muller P 2010 Correlation reflectometry at TEXTOR *Rev. Sci. Instrum* **81** 113502

[18] Qu H *et al* 2015 Radial and poloidal correlation reflectometry on experimental advanced superconducting tokamak *Rev. Sci. Instrum.* **86** 083503

[19] Krämer-Flecken A *et al* (the W7-X team) 2017 Investigation of turbulence rotation in limiter plasmas at W7-X with newly installed poloidal correlation reflectometer *Nucl. Fusion* **57** 066023

[20] Windisch T, Krämer-Flecken A, Velasco J L, Könies A, Nührenberg C, Grulke O, Klinger T and the W7-X team 2017 Poloidal correlation reflectometry at W7-X: radial electric field and coherent fluctuations *Plasma Phys. Control. Fusion* **59** 105002

[21] Gusakov E Z and Popov A Y 2006 Measurements localization in poloidal correlation reflectometry *Nucl. Fusion* **46** S829–35

[22] Prisiazhniuk D 2017 Development and application of poloidal correlation reflectometry to study turbulent structures in the ASDEX Upgrade tokamak *PhD Thesis* Technical University Munich, Germany (https://doi.org/10.14459/2017md1353097)

[23] Prisiazhniuk D, Krämer-Flecken A, Conway G D, Happel T, Manz P, Simon P, Stroth U and the ASDEX Upgrade Team 2015 Application of poloidal correlation reflectometry to study turbulence at ASDEX Upgrade *Proc. 12th Int. Reflectometry Workshop—IRW12 (Jülich)*

[24] Maj O, Pereverzev G V and Poli E 2009 Validation of the paraxial beam-tracing method in critical cases *Phys. Plasmas* **16** 062105

[25] Maj O, Balakin A A and Poli E 2010 Effects of aberration on paraxial wave beams: beam tracing versus quasi-optical solutions *Plasma Phys. Control. Fusion* **52** 085006

[26] Bretz N 1992 One-dimensional modeling of the wavelength sensistivity, localization, and correlation in reflectometry measurements of plasma fluctuations *Phys. Fluids* **4** 2414

[27] Fanack C, Boucher I, Clairet F, Heuraux S, Leclert G and Zou X L 1996 Ordinary-mode reflectometry: modification of the scattering and cut-off responses due to the shape of localized density fluctuations *Plasma Phys. Control. Fusion* **38** 1915

[28] Gusakov E, Heuraux S, Popov A and Schubert M 2012 Reconstruction of the turbulence radial profile from reflectometry phase root mean square measurements *Plasma Phys. Control. Fusion* **54** 045008

[29] Gusakov E Z *et al* 2002 Small-angle scattering and spatial resolution of fluctuation reflectometry: comparison of 2D analytical theory with numerical calculations *Plasma Phys. Control. Fusion* **44** 1565

[30] Conway G D, Schirmer J, Klenge S, Suttrop W, Holzhauer E and the ASDEX Upgrade Team 2004 Plasma rotation profile measurements using Doppler reflectometry *Plasma Phys. Control. Fusion* **46** 951

[31] Conway G D, Poli E, Happel T and the ASDEX Upgrade Team 2010 Interaction of mean and oscillating plasma flows across confinement mode transitions *Plasma Fusion Res.* **5** S2005

[32] Conway G D, Angioni C, Dux R, Ryter F, Peeters A G, Schirmer J, Troester C and CFN Reflectometry Group and the ASDEX Upgrade Team 2006 Observations on core turbulence transitions in ASDEX Upgrade using Doppler reflectometry *Nucl. Fusion* **46** S799–808

[33] Lebschy A *et al* 2017 *Plasma Phys. Control. Fusion* **58** 026013

[34] Prisiazhniuk D, Manz P, Conway G D, Happel T, Krämer-Flecken A, Stroth U and the ASDEX Upgrade Team 2017 Measurement of the turbulent phase velocity in the L-mode edge of ASDEX Upgrade and comparison with GEMR simulations *44th EPS Conf. on Plasma Physics (Belfast)*

[35] Manz P, Prisiazhniuk D, Happel T, Freethy S, Scott B D, Stroth U and the ASDEX Upgrade Team 2018 On the phase velocity in between weak and strong plasma edge turbulence *Plasma Phys. Control. Fusion* submitted

[36] Xin Z and Guo-Wei H 2009 Space-time correlations of fluctuating velocities in turbulent shear flows *Phys. Rev.* **79** 046316

[37] Terry P W 2010 Suppression of turbulence and transport by sheared flow *Rev. Mod. Phys.* **72** 109

[38] Nagashima Y *et al* (the JFT-2M group) 2007 In search of zonal flows by using direct density fluctuation measurements *Plasma Phys. Control. Fusion* **49** 1611–25

[39] Conway G D, Scott B, Schirmer J, Reich M, Kendl A and the ASDEX Upgrade Team 2005 Direct measurement of zonal flows and geodesic acoustic mode oscillations in ASDEX Upgrade using Doppler reflectometry *Plasma Phys. Control. Fusion* **47** 1165–85

[40] Draper N and Smith H 1998 *Applied Regression Analyses* (New York: Wiley-Interscience)

[41] Poli E, Peeters A G and Pereverzev G V 2001 TORBEAM, a beam tracing code for electron-cyclotron waves in tokamak plasmas *Comput. Phys. Commun.* **136** 90

[42] Gusakov E Z and Popov A Y 2002 Nonlinear theory of fluctuation reflectometry *Nucl. Fusion* **44** 2327–37

[43] Piliya A D and Popov A Y 2002 On the application of the reciprocity theorem to calculation of a microwave radiation signal in inhomogeneous hot magnetized plasma *Plasma Phys. Control. Fusion* **44** 467

[44] Bulanin V V and Yafanov M V 2006 Spatial and spectral resolution of the plasma Doppler reflectometry *Plasma Diagn.* **32** 41

[45] Hutchinson I H 1992 One-dimensional full-wave analysis of reflectometry sensitivity and correlations *Plasma Phys. Control. Fusion* **34** 1225

[46] Mc Carthy P J and the ASDEX Upgrade Team 2012 Identification of edge-localized moments of the current density profile in a tokamak equilibrium from external magnetic measurements *Plasma Phys. Control. Fusion* **54** 015010

[47] Soldatov S *et al* 2009 Investigation of the poloidal spectral resolution of O-mode reflectometry with two-dimensional full-wave modeling *Fusion Eng. Des.* **84** 64

[48] Lin Y, Nazikian R, Irby J H and Marmar E S 2001 Plasma curvature effects on microwave reflectometry fluctuation measurements *Plasma Phys. Control. Fusion* **43** L1

[49] Hirsch M and Holzhauer E 2004 Doppler reflectometry with optimized temporal resolution for the measurement of turbulence and its propagation velocity *Plasma Phys. Control. Fusion* **46** 593